2011

Transport Properties of Nanometer-sized Assemblies through Nanofluidic Channels with Single Entity Electrical Detection

Franklin Ifeanyichukwu Uba
Louisiana State University and Agricultural and Mechanical College, fuba1@tigers.lsu.edu

TRANSPORT PROPERTIES OF NANOMETER-SIZED ASSEMBLIES THROUGH NANOFLUIDIC CHANNELS WITH SINGLE ENTITY ELECTRICAL DETECTION

A Thesis

Submitted to the Graduate Faculty of the
Louisiana State University and
Agricultural and Mechanical College
in partial fulfillment of the
requirements for the degree of
Master of Science

in

The Department of Chemistry

by
Franklin Ifeanyichukwu Uba
B.Sc Hons, University of Ibadan, 2007
August, 2011

DEDICATION

To God be the glory great things he has done.

I dedicate this work to my lovely family for their support and prayers.

ACKNOWLEDGEMENTS

I would like to express my sincere gratitude to my advisor, Prof. Steven Allan Soper for his unwavering support and encouragement throughout this research work. His help has made this work a success. I am also grateful to the members of my thesis committee, Prof. Kermit K. Murray and Prof. George G. Stanley for their time, support and contributions towards the realization of my degree.

I would also not like to forget to thank Prof. Yoon-kyoung Cho for the invitation to embark on this research work in conjunction with the World Class University (WCU) program at UNIST. I also thank Mr. Dong-kyu Park of UNIST for his help.

I also appreciate members of the Soper research group, most importantly postdoctoral Research Associates (Dr. Chantiwas, Dr. Hupert, Dr. Witek, Dr. Wang) and senior colleagues (Dr. Njoroge and Dr. Dharmasiri), for helpful contributions.

Thank you all.

TABLE OF CONTENTS

LIST OF TABLES

LIST OF FIGURES

LIST OF SCHEMES

ABBREVIATIONS AND ACRONYMS

AC	-	Alternating Current
B	-	Bandwidth (Hz)
C_{eq}	-	Equivalent Concentration
C_i	-	Bulk ionic Concentration of solution (mol/dm^3)
Cyt c	-	Cytochrome c
DC	-	Direct current
DL	-	Diffuse Layer
DLVO	-	Derjaguin, Landau, Verwey and Overbeek
DNA	-	Deoxyribonucleic acid
DRIE	-	Deep Reactive Ion Etching
D_u	-	Dukhin number
E	-	Electric Field strength (volts per centimeter or V/cm)
EDL	-	Electric Double Layer
EDTA	-	Ethylene Diamine Tetra Aceticacid
EKP	-	Electrokinetic Phenomena
EOF	-	Electroosmotic flow
eV	-	electron Volt (1 eV = 1.6026×10^{-19} J)
F	-	Faraday's Constant (96,485 C/mol)
F_d	-	Drag Force (N)
F_e	-	Electrical force (newton/N)
FIB	-	Focused Ion Beam
FITC	-	Fluorescein Isothicyanate
G	-	Conductance (Ω^{-1} or siemens)
g	-	Acceleration due to gravity ($9.8ms^{-2}$)
G_b	-	Conductivity of Buffer
h	-	Channel height
I	-	Ionic strength of electrolytes
$I_{cond, bulk}$	-	Conduction Current from Bulk solution conductivity (A)
$I_{cond, surf}$	-	Conduction Current from Surface conductivity (A)

I_t	-	Tunneling Current
k_B	-	Boltzmann constant (1.38 x 10^{-23} JK^{-1})
L	-	Nanogap size
l_p	-	Persistence length (nm)
L_{cont}	-	Contour length
LDOS	-	Local Density of States
m	-	Mass of electron (9.10938188 x 10^{-31} kg)
n	-	Refractive index
N_A (mol^{-1})	-	Avogadro's number of molecules /ions (6.02214 x 10^{23})
PDMS	-	Poly (dimethylsiloxane)
Q	-	Volume Flow rate (liter per min)
q_e	-	Electron Charge (1.602 x 10^{-9} C)
q_i	-	Ionic charge
R ($JK^{-1}mol^{-1}$)	-	Molar Gas constant
r_i	-	Geometrical Radius of Hydrated ion
rms	-	Root-Mean-Square
RNA	-	Ribonucleic acid
SL	-	Stern Layer
T	-	Kelvin Temperature (Kelvin or K)
TBE	-	Tris(hydroxymethyl)aminomethane-borate-EDTA
u_i	-	Effective Ionic Mobility (m^2/sV)
u_i^{∞}	-	Absolute Ionic mobility
V (volts)	-	Applied Voltage
v_{eof} ($cm\ s^{-1}$)	-	Electrophoretic velocity
v_{ep}	-	Electrophoretic velocity
z_i	-	Ionic Charge
ΔE	-	Activation energy (kJ/mol)
ΔG	-	Change in conductivity
Δp (Atm)	-	Pressure drop
ΔV (volts)	-	Voltage drop

ε_0	-	Electrical permittivity of vacuum
ε_e	-	Electrical Permittivity of a medium
ε_r	-	Relative dielectric constant
ε_w	-	Dielectric permittivity of solvent (usually water)
ζ (mV)	-	Zeta Potential
η	-	Dynamic Viscosity of solution
κ	-	Electrical Conductivity (siemens per centimeter or S/cm)
κ_b	-	Bulk electrolyte conductivity ($\Omega^{-1}m^{-1}$)
κ_d	-	Debye-Hückel parameter
κ_s	-	Surface conductivity ($\Omega^{-1}m^{-1}$)
Λ	-	Solution Molar Conductivity
λ_-	-	Molar Conductivity of Anions
λ_+	-	Molar Conductivity of Cations
λ_d	-	Debye Length
μ_{eof}	-	Electroosmotic flow mobility ($cm^2\ V^{-1}\ s^{-1}$)
μ_{ep}	-	Electrophoretic mobility ($cm^2\ V^{-1}\ s^{-1}$)
v_{eof} (cms^{-1})	-	Electroosmotic Flow Velocity
ξ	-	Stokes drag (Ns/m)
ρ (Ω cm)	-	Resistivity at a temperature T
σ (gcm^{-3})	-	Density
Ψ_x	-	Potential of Plane at a distance x
$\hbar$	-	Planck's Constant

ABSTRACT

Recently, there have been reports on biological and solid-state nanopores that identify single biopolymers or their constituent monomers by analyzing changes in ionic current blockades when they block the flux of buffer ions while travelling through the nanopores. Nevertheless, there have been several limitations in their application, especially as DNA detectors; Poor confinement of the DNA strand within the nanopore (~0.1 % of a 10 kilobase (kb) DNA), poor signal sensitivity and random motion experienced by the DNA in solution that results in a large amount of noise in the signal. These have led to the development of nanochannel-based devices, which can directly address the aforementioned challenges.

Nanochannels have widths comparable to nanopores but with longer lengths. As molecules travel through nanochannels, they undergo confinement, hydrophobic and van der Waals interactions with the walls of the channel generating some interesting physics, such as the elongation of DNA molecules. The small scale analyses offer high throughput with interesting attributes not accessible at the micro-scale.

Presently, an expanding research area involves the integration of nanochannels with nanogap electrodes to provide new transduction modalities for single molecules traveling through nanochannels. In these detectors, the electrical behavior (field effect, impedance, capacitance, resistance, conductance, etc.) of biomolecules are observed. These have become powerful tools for bio-sensing, single molecule manipulation and design of high throughput systems, for example as systems for DNA sequencing.

This work focuses on developing a novel technique for the fabrication of mixed-scale systems (nm to mm) in quartz used for the molecular-scale sensing of single-

molecules (DNAs, RNAs, peptides and proteins). These systems consist of both microchannels and nanochannels (10-100 nm). Results on the fabrication of such systems will be reported. I will also discuss our ultimate goal; to develop a platform for the rapid and efficient sequencing of biopolymers by measuring flight-times of monomer units clipped from a single polymer digested with an enzyme. The flight times will be transduced using a non-labeling electrical approach via conductivity in a detection volume defined by nano-scale electrodes (5-10 nm). Theoretical computations performed to describe the variation of the Signal-to-Noise with the nano-electrode area and nano-gap size have provided promising results.

CHAPTER 1. INTRODUCTION

1.1 Nanofluidics and DNA Sequencing

Many fundamental processes of biology, for example, information storage, transcription, translation, gene regulation, mitosis, and cell communication occur on the micrometer to nanometer scale.[1,2,3,4] Using micro- and nanofabrication technologies developed for the microelectronics industry, devices can readily be made on these length scales, thus enabling studies of single molecules and cells on a size-scale comparable to molecular dimensions. In addition, new analysis tools for single-molecules can be realized using devices with micro- and nanometer scale structures.

Miniaturization of analytical devices has been an ongoing trend with the impetus focused on improving the performance of these analytical tools. The general benefits of miniaturization are the use of less reagents, parallel analysis, faster operation, and more sensitive detection.[5] More interesting are the new qualitative possibilities that include:[6] Single-cell analysis by integration of several biochemical steps into a micro total analysis system (μTAS); high-resolution analysis using local light sources and detectors or local electrical detection; and direct manipulation of relevant bio-entities such as proteins, nucleic acids, bio-molecular complexes and organelles such as ribosomes and mitochondria and even whole cells.

An important field that lies at the interface between engineering, chemistry and biology that has been applied in the development of methods for the analysis of biological and biochemical system is microfluidics.[5,7] Microfluidics is the science and technology that process or manipulate small amounts of fluids using channel systems with dimensions on the micrometer scale (100 μm to sub-micrometer).[8]

Although miniaturization to the micrometer-scale opens up the possibility to probe biology at the single cell level, many fundamental biological processes, such as the epigenetic and genetic control of single cells, have been observed to take place at the molecular level (*i.e.,* nano-scale). Therefore, downsizing micro-fluidic channels to the nanometer-scale can provide information that cannot be realized in micro-scale domains.

This has led to the emergence of a new field called nanofluidics.[9,10] Nanofluidics involves the study of fluid flows in structures with at least one dimension approaching the nanometer range. While microfluidics has been reserved for dimensions in the range from 100 nm to 100 μm, dimensions in the range of 1 - 100 nm have been coined nanofluidics.[11] Although, scientists in the past have extensively studied transport properties on fluids in the nano-scale, it is not until the last several years that this field was coined.[12] The invention and wide availability of many new technological tools like atomic force microscope (AFM)[13] and scanning tunneling microscope (STM)[14,15] (both for inspection and creation of nanostructures), electron[16] and ion-beam lithographs[17,18] and the development of new nanomachining techniques like soft lithography,[19,20] bottom-up assembly methods[21] and surface science apparatus (SFA)[22] has made the study and application of nanofluidics much more accessible.

Fluid conduits with at least one dimension from 1 nm to 100 nm have been reported. These include reports such as nanopores in zeolite crystals[23] and nuclear membranes of biological cells to larger openings in the silica frustules of diatoms.[24,25] Nanoporous inorganic structures have resulted from the atomic arrangement of components.

A multidisciplinary approach is essential when performing nanofluidics. Eijkel *et al*.[12] in his review article reported the schematic diagram, shown in Figure 1.1, indicating a great number of classical disciplines where knowledge on nanofluidics is currently being applied. A unique feature of nanofluidics is that the relevant length scale is comparable to the range of surface and interfacial forces in liquids, such as electrostatic, van der Waals and steric interactions. Molecular simulations are an effective tool for elucidating the discreteness of molecules also to describe ion transport within nanochannels.[26] Li *et al.* published an extensive review article on molecular simulations of nanoscale liquid flow.[27]

Recently, scientists have embarked upon applying the field of nanofluidics to DNA sequencing. Good knowledge of the base sequence of specific DNAs can significantly contribute not only to the understanding of pathogens and diseases, but also to drug discovery and early diagnosis of diseases for personalized medicine.[28] These benefits were highlighted in the Nobel lectures and reports of Walter Gilbert[29,30] and Fredrick Sanger.[31,32,33]

1.2 Deoxyribonucleic Acid (DNA)

In their 1953 article published in *Nature* entitled 'Molecular Structure of Nucleic acids',[34] James Watson and Francis Crick described Deoxyribonucleic Acid (DNA) as a long biopolymer composed of repeating units called nucleotides and also comprised of two negatively charged backbones intertwined in a double helical structure. This extensive report formed the basis for the 1962 shared Nobel prize in Physiology or Medicine awarded to J.D Watson, F. H Crick and M. H Wilkins (Figure 1.2a). Each

backbone is coiled around the same axis and has a pitch of 34 Å (3.4 nm) and a radius of 10 Å (1.0 nm) as shown in Figure 1.2b.

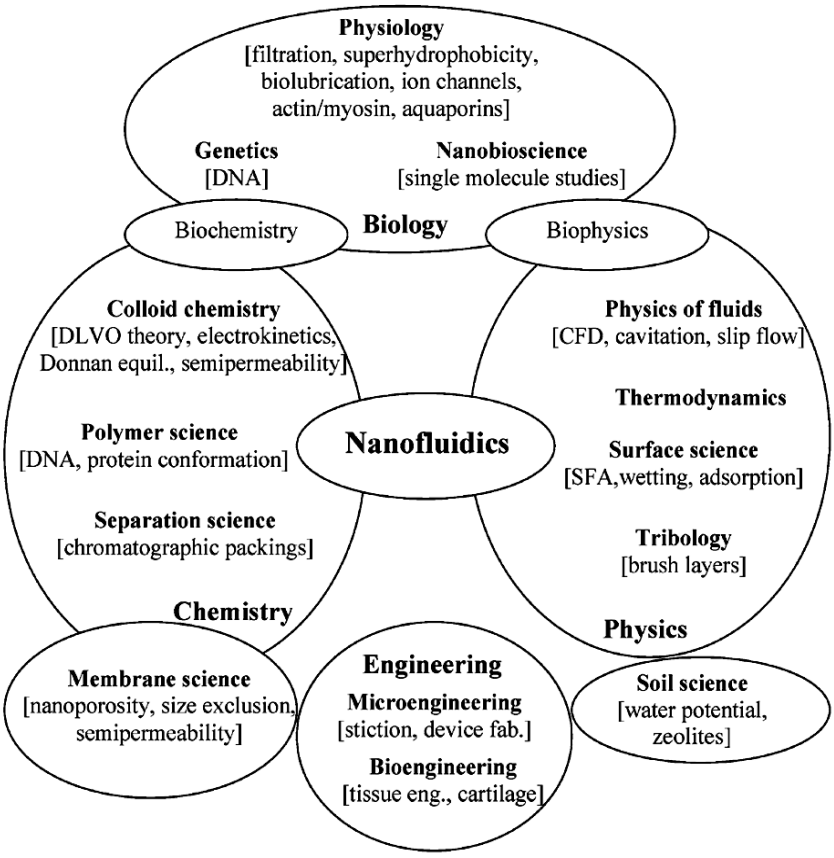

Figure 1.1 Classical disciplines relevant to nanofluidics and the different phenomena. Reproduced from Reference [12] with permission.

DNA is a natural polymer that can be found in all plants and animal cells. In human cells, it resides within the nucleus and mitochondria and is responsible for the encryption and transmission of hereditary information. A nucleotide unit of DNA is composed of a nitrogenous base, a five-carbon 2'-deoxyribose sugar and one to three phosphate groups. These phosphate groups can form bonds with carbon 2, 3 or 5 of the sugar groups.

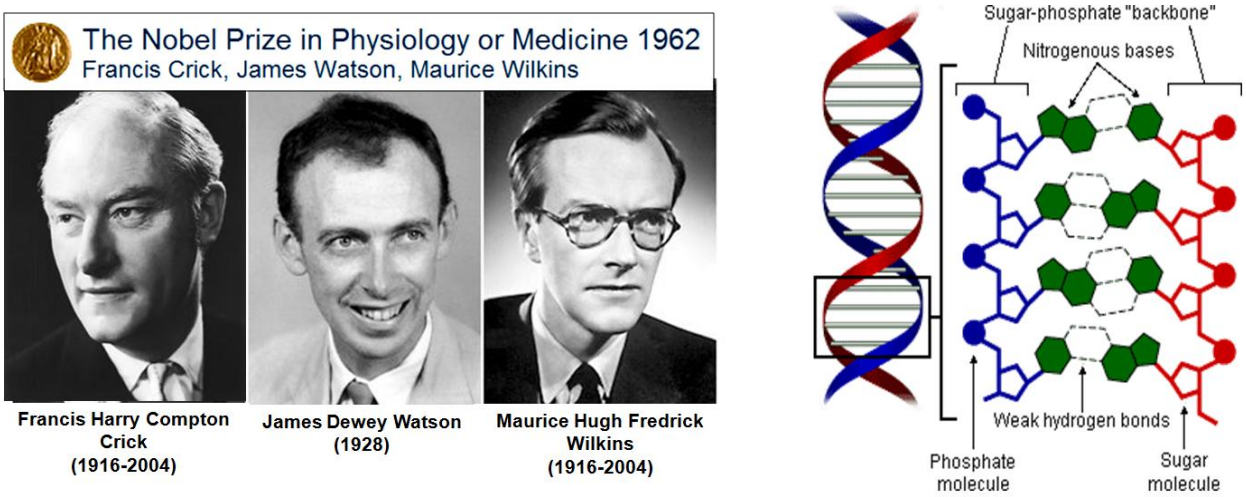

Figure 1.2 (from left to right) F.H. Crick, J.D. Watson and M.H. Wilkins; 1962 Noble prize recipients in Physiology or Medicine and DNA structure as described by Watson and Crick.

The nucleotides can be categorized depending on the number of phosphate groups they possess;

- Deoxynucleotide monophosphate (dNMPs) – contains *one* phosphate group bonded to the ribose sugar.
- Deoxynucleotide diphosphate (dNDPs) – contains *two* phosphate groups bonded to the ribose sugar
- Deoxynucleotide triphosphate (dNTPs) – contains *three* phosphate groups bonded to the ribose sugar

The nitrogenous bases are grouped into pyrimidines (heterocyclic aromatic organic compound containing two nitrogen atoms at positions 1 and 3 of the six-membered ring) and purines (heterocyclic aromatic organic compound, consisting of a pyrimidine ring fused to an imidazole ring). Purines present in DNA are Adenine-A and Guanine-G while the pyrimidines are Thymine-T and Cytosine-C. Figure 1.3 shows the structures of the four nitrogenous bases of DNA.

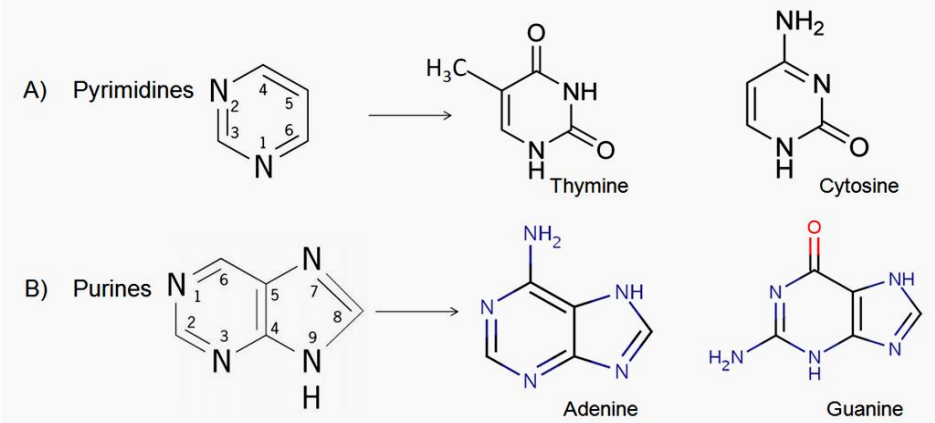

Figure 1.3 (A) Pyrimidine and (B) Purine functional group rings and the structures of each form present in DNA

In DNA, the nitrogenous bases are bound in specific sequences that govern the primary structure and folding of proteins. These proteins form the elementary building blocks in living organisms. The backbones of double-stranded DNAs are held together by the bases that pair-up in a manner in which A binds to T and G binds to C; hence, the backbones become complementary. This is referred to as 'Watson-Crick base pairing'. DNA molecule can be very long, consisting of several hundred million base-pairs (bp) with each base-pair contributing 0.34 nm to the total length of the molecule. The lengths can extend from several centimeters to meters. In living cells, the DNA is organized into chromosomes (see Figure 1.4), which can be linear or circular depending upon the type of cell. The set of chromosomes in a cell make up the total genome. The human genome, with 3 billion base pairs, extends approximately 1.8 m in length and is arranged into 46 chromosomes.[35]

1.2.1 Chemical Make-up of DNA

The backbone of the DNA biopolymer is made up of two types of structures – β-D-2-deoxyribose and phosphate groups. Deoxyribose sugar is a modification of the

ribose sugar in which the –OH group on position 2' of the ribose sugar has been replaced by a hydrogen (see Figure 1.5). A complete schematic for DNA polymer chemistry is shown in Figure 1.6.

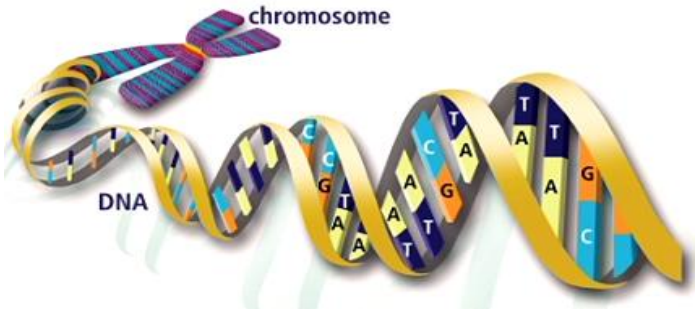

Figure 1.4 Organization of DNA into Chromosomes.

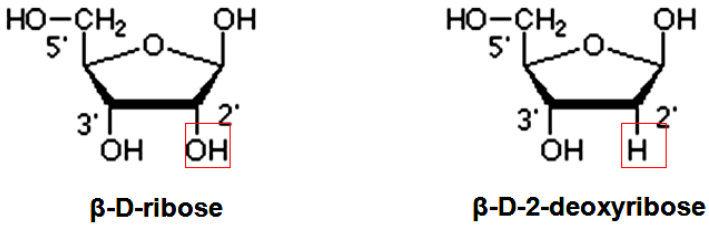

Figure 1.5 Molecular Structures of β-D-Ribose and β-D-2-Deoxyribose Sugar Units

The 2-deoxyribose units of the DNA are covalently linked together with intermittent phosphate groups to form a long polymer chain with the release of water molecules. This type of polymerization is referred to as condensation polymerization. Phosphodiester bonds are formed between the 3' oxygen of one sugar and the 5' oxygen of the next with the release of one water molecule per linkage. Repeated polymerization results in the formation of the long chain DNA backbone (see Figures 1.6 A and B).

The secondary amine group located at position 1 of the nitrogeneous bases forms a strong covalent bond with the carbon 1' (anomeric carbon) of the deoxyribose

sugar. Here, the secondary amine nitrogen of the base acts as the nucleophile rather than the oxygen of the alcohol (Figure 1.6B). Each molecule is a single long strand, held together by the covalent bonds along its backbone. Each strand is connected to each other by hydrogen bonds between the bases. Although hydrogen bonds are much weaker than covalent bonds, there are many hydrogen bonds connecting the two DNA strands in the double helix and as such, they serve well to maintain that structure until there is a need for separation of the two chains. Not only do the hydrogen bonds hold the chains together, they are also very specific in which bases are connected by the hydrogen bonds and the number of hydrogen bonds between each base pair.

Adenine (A) forms two hydrogen bonds with thymine (T) while Guanine (G) forms three hydrogen bonds with cytosine (C) (see Figure 1.6 C). The hydrogen bond in each case is formed between the positive hydrogen end of a polar N-H bond and a pair of electrons on either nitrogen or carbonyl oxygen. In these "complementary" base pairs, a purine base always bonds to a pyrimidine base. This means that the distance between the two backbones is always the same (*i.e*., three rings - two from purine and one from pyrimidine - and the hydrogen bonds). Hydrogen bonding between two purine bases, for example, would put four rings into the base pair and will result in a poor fit.

1.3 Miniaturized Devices and DNA Sequencing

The design of lab-on-a-chip devices, which can make the sequencing of DNA faster and cheaper, will have high impact in the fields of Biology, Chemistry, Medicine and Biomedical Engineering. Over the years, nanopores have been potential candidates for devices specifically for DNA sequencing. Nanopores have been regarded as structures whose pore depth is comparable to its diameter. They have aided in the

study of the transport properties of different ions or molecules in a confined space. Initial experiments involved the use of the biological nanopore, α-hemolysin (Figure 1.7a) for single DNA polynucleotide detection (Figure 1.7b).[36]

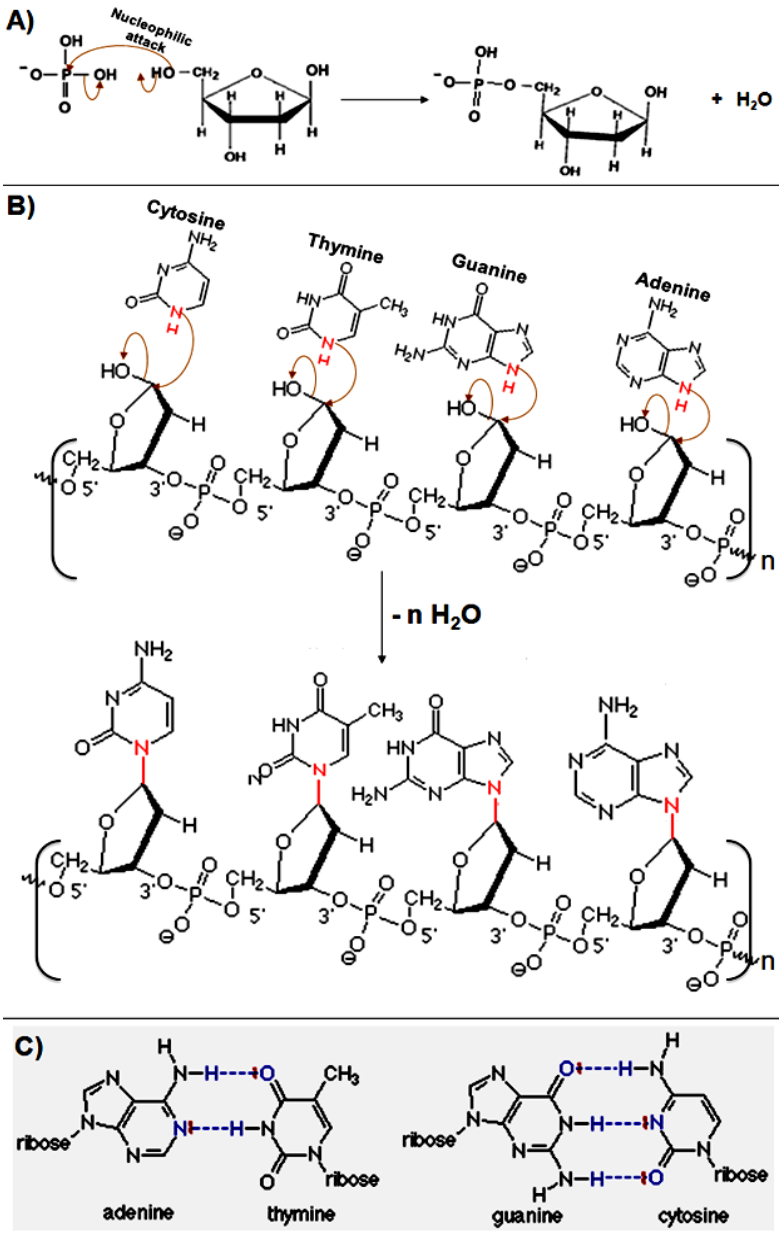

Figure 1.6 Polymer Chemistry of DNA Molecule (A) Shows the mechanism of nucleophilic attack of The electron deficient phosphate by the electron rich –OH of ribose and (B) Mechanism of nucleophilic attack of sugar by the nitrogeneous base, accompanied by water loss.

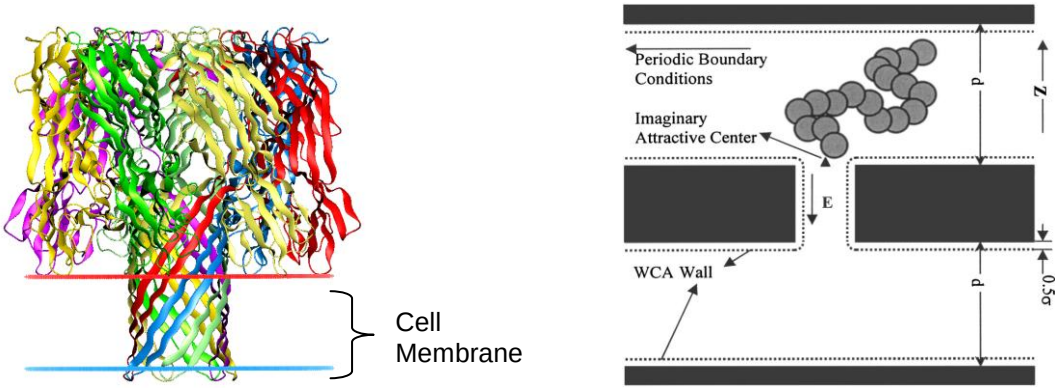

Figure 1.7(A) α-hemolysin 3-dimensional structure (B) brownian dynamics of DNA translocation through nanopores.

Meller *et al*.[37] and Kasianowicz *et al*.[38] extensively studied the application of both biological and solid-state nanopores in differentiating single nucleotides by analyzing changes in ionic current blockade amplitudes when single nucleotides exclude buffer ions when travelling through these pores. Although nanopores have served as potential candidates for the design of devices for DNA sequencing, they experience some limitations. Liang *et al*.[39] pointed out that random motion experienced by the DNA in solution, results in a large amount of noise in the ionic current.

These limitations have led to the development of nanochannel-based devices. Nanochannels have widths comparable to that of nanopores, but with extremely longer lengths (depths). As molecules travel through nanochannels, they undergo hydrophobic and van der Waals interactions with the walls of the channel. The small scale analyses with low sample volumes and reduced processing times at the dimensions associated with nanochannels offers high throughput capabilities. Therefore, the need for developing efficient and cost-effective nanofabrication methods arose.

In recent times, researchers have suggested the use of nanochannels for direct physical models of ionic channels in cells thereby making the fabrication of

nanochannels gain immense significance.[40] By mimicing or harnessing these localized effects, one can gain control over molecular motion. Several attempts have been reported in the literature that take advantage of the limited dimensions of nanochannels to restrict or prevent the motion of otherwise globular molecules through the nanochannels.[41,42]

Nanochannels offer great flexibility in terms of shape and size, increased robustness and surface properties, which can be tuned based on the required function.[43,44,45] Several methods of nanochannel fabrication on silicon, silica and glass substrates have been reported in the literature.[46] Each scheme employed depends on the nature and required geometry of the substrate material. Fabrication protocols for fused silica substrates for nanofluidic devices have been well established and reported.[47,48] The choice of fused silica in our experiments has been primarily due to its good optical properties, environmental stability, accommodation of many nanofabrication techniques and compatibility with biological systems.

Presently, a continually expanding research area involves the integration of nanochannels with nanogap electrodes as potential devices for biological sensing. These have become powerful tools for biosensing, single-molecule manipulation and the design of high throughput systems for DNA sequencing.[49] Nanogap electrodes are defined as a pair of electrodes with a nanometer gap.[50] In these detectors, the electrical behavior (field effect, impedance, capacitance, resistance, conductance, *etc.*) of biomolecules are observed and used in detecting them when the molecule is resident within the nanosized gaps. A recent review by Chen *et al*.[51] enumerated several planar nanogaps (nanogaps in which electrodes face each other horizontally in the device). In

2008, Liang *et al.*[39] described the fabrication and characterization of a planar nanogap detector within a 45 x 45 nm fluidic channel (50 μm length, 45 nm width and 45 nm depth) integrated with a pair of perpendicular metal electrodes of 45 nm width and 18 nm thickness with gap sizes ranging from 9 to 20 nm and heights 16 to 30 nm, respectively. Although the authors observed electrical signals generated by 1.1 kbp ds DNA passing through the nanogap detector, they suggested the optimization of the dimensions, DNA flow speed across the channel and fluctuations in DNA. This has formed a solid foundation for our current work.

1.4 Objective of the Project

The objective of this work was to design, fabricate and characterize the operation of an integrated fluidic system that will serve as the foundation for a novel DNA sequencing system based on Time-of-Flight (ToF) measurements of single mono-nucleotides clipped from a double-stranded DNA biopolymer digested with a λ-exonuclease enzyme. The flight times will be transduced using a non-labeling electrical approach via conductivity in a detection volume defined by nano-scale electrodes (5-10 nm). This platform will be useful for molecular-scale sensing of single-molecules, such as RNAs, peptides and proteins. The integrated fluidic system is comprised of two microfluidic access channels and a nanofluidic channel (50 μm in length; 50 x 50 nm, width x depth) containing two pairs of transverse Au nano-electrodes poised at the input/output ends of the nanochannel.

The nanochannel possesses a funnel entrance populated with nanopillars to reduce entropic barriers, which allows for the efficient entry of single molecules into the nanochannel. The nanoelectrodes transduce the ToF of single mononucleotides

entering and exiting a single flight tube (nanochannel). The respective flight times will depend upon the characteristic structure of the molecule in addition to hydrophobic, van der Waals and/or electrostatic interactions with functional groups on the wall of the nanochannels. Novel techniques are being used for the fabrication of these mixed-scale systems (nm to mm) in quartz substrates.

Theoretical computations are based upon single mononucleotide units, which have been used to show that the nanogap size as well as the bias voltage between the electrode pairs has a profound impact on the signal-to-noise ratio for transducing single mononucleotides. These computations are being used to guide the fabrication of the prototype device.

1.5 Report Outline

A summary of the contents of the chapters in this dissertation is presented below:

Chapter 2 Theory

In order for the reader to understand the concept of current blockages, electrical measurements of single-molecules traversing through a pair of nano-gap electrodes and ToF measurements, Chapter 2 gives a description of the basic concepts of the electrical double layer, electrophoresis and electro-osmosis. It also presents the concept of DNA confinement, stretching and volume exclusion. Introduction to the concept of nanogap detection is also provided and concludes by describing DNA as a model polymer for nanogap measurements.

Chapter 3 Fabrication and electrical properties of a nanogap device

This chapter presents the methods for the device design, delineates the fabrication protocols and describes the electrical properties of the nanogap device. It also describes the experimental methods in detail.

Chapter 4 Results, discussions, conclusions and future works

This chapter discusses the experimental results of the nanogap device and provides the future applications for the nanofluidic device.

1.6 References

1. Lockhart, D. J.; Winzeler, E. A., Genomics, gene expression and DNA arrays. *Nature* **2000,** *405* (6788), 827-836.
2. Manz, A.; Graber, N.; Widmer, H. M., Miniaturized total chemical-analysis systems - a novel concept for chemical sensing. *Sensor and Actuat. B-Chem.* **1990,** *1* (1-6), 244-248.
3. Adams, A. A.; Okagbare, P. I.; Feng, J.; Hupert, M. L.; Patterson, D.; Göttert, J.; McCarley, R. L.; Nikitopoulos, D.; Murphy, M. C.; Soper, S. A., Highly Efficient Circulating Tumor Cell Isolation from Whole Blood and Label-Free Enumeration Using Polymer-Based Microfluidics with an Integrated Conductivity Sensor. *J. Ame. Chem. Soc.* **2008,** *130* (27), 8633-8641.
4. Dharmasiri, U.; Witek, M. A.; Adams, A. A.; Soper, S. A., Microsystems for the Capture of Low-Abundance Cells. *Annu. Rev. of Anal. Chem.* **2010,** *3* (1), 409-431.
5. Wood, J., Microfluidics begins to realize its potential - Micro/nanofluidics. *Nano Today* **2007,** *2* (1), 16-16.
6. Tegenfeldt, J. O.; Prinz, C.; Cao, H.; Huang, R. L.; Austin, R. H.; Chou, S. Y.; Cox, E. C.; Sturm, J. C., Micro- and nanofluidics for DNA analysis. *Anal. and Bioanal. Chem.* **2004,** *378* (7), 1678-1692.
7. Kenis, P. J. A.; Stroock, A. D., Materials for micro- and nanofluidics. *Mrs Bulletin* **2006,** *31* (2), 87-94.
8. Whitesides, G. M., The origins and the future of microfluidics. *Nature* **2006,** *442* (7101), 368-373.
9. Foquet, M.; Korlach, J.; Zipfel, W. R.; Webb, W. W.; Craighead, H. G., Focal Volume Confinement by Submicrometer-Sized Fluidic Channels. *Anal. Chem.* **2004,** *76* (6), 1618-1626.
10. Tegenfeldt, J. O.; Prinz, C.; Cao, H.; Chou, S.; Reisner, W. W.; Riehn, R.; Wang, Y. M.; Cox, E. C.; Sturm, J. C.; Silberzan, P.; Austin, R. H., The dynamics of

genomic-length DNA molecules in 100-nm channels. *PNAS* **2004,** *101* (30), 10979-10983.

11. Abgrall, P.; Nguyen, N. T., Nanofluidic Devices and Their Applications. *Anal. Chem.* **2008,** *80* (7), 2326-2341.

12. Eijkel, J. C. T.; van den Berg, A., Nanofluidics: what is it and what can we expect from it? *Micro. and Nanoflu.* **2005,** *1* (3), 249-267.

13. Giessibl, F. J., Advances in atomic force microscopy. *Revs. of Mod. Phys.* **2003,** *75* (3), 949.

14. Tersoff, J.; Hamann, D. R., Theory of the scanning tunneling microscope. *Phys. Rev. B* **1985,** *31* (2), 805.

15. Binnig, G.; Rohrer, H.; Gerber, C.; Weibel, E., Surface Studies by Scanning Tunneling Microscopy. *Phys. rev. lett.* **1982,** *49* (1), 57.

16. Broers, A. N.; Hoole, A. C. F.; Ryan, J. M., Electron beam lithography--Resolution limits. *Microelect. Eng.* **1996,** *32* (1-4), 131-142.

17. Marrian, C. R. K.; Dobisz, E. A.; Dagata, J. A., Electron-beam lithography with the Scanning tunneling microscope. *J. Vac. Sci. & Tech.* **1992,** *10* (6), 2877-2881.

18. Dobisz, E. A.; Marrian, C. R. K., Sub-30-nm lithography in a negative electron-beam resist with a vacuum scanning tunneling microscope. *Appl. Phys. Lett.* **1991,** *58* (22), 2526-2528.

19. Whitesides, G. M.; Gates, B.; Mayers, B.; Xu, Q. B., Soft lithography and nanofabrication. *Abstr. Ame. Chem. Soc.* **2005,** *229*, 204.

20. Qin, D.; Xia, Y. N.; Whitesides, G. M., Soft lithography for micro- and nanoscale patterning. *Nat. Prot.* **2010,** *5* (3), 491-502.

21. Du, Y.; Lo, E.; Vidula, M. K.; Khabiry, M.; Khademhosseini, A., Method of Bottom-Up Directed Assembly of Cell-Laden Microgels. *Cell and Molec. Bioeng.* **2008,** *1* (2-3), 157-162.

22. Derjaguin, B. V.; Titijevskaia, A. S.; Abricossova, II; Malkina, A. D., Investigations of the forces of interaction of surfaces in different media and their application to the problem of colloid stability. *Dis. Faraday Soc.* **1954,** (18), 24-41.

23. Salavati-Niasari, M., Host (nanopores of zeolite-Y)/guest (Ni(II)-tetraoxo dithia tetraaza macrocyclic complexes) nanocomposite materials: template synthesis and characterization. *J. Inclus. Phen. and Macrocyclic Chem.* **2008,** *62* (1-2), 65-73.

24. Mazumder, N.; Gogoi, A.; Kalita, R. D.; Ahmed, G. A.; Buragohain, A. K.; Choudhury, A., Luminescence studies of fresh water diatom frustules. *Indian J. Phys.* **2010,** *84* (6), 665-669.

25. Yamanaka, S.; Yano, R.; Usami, H.; Hayashida, N.; Ohguchi, M.; Takeda, H.; Yoshino, K., Optical properties of diatom silica frustule with special reference to blue light. *J. Appl. Phys.* **2008,** *103* (7).

26. Chen, M.; Chen, Y.; Zhong, W.; Yang, J., Molecular dynamics simulation of ion transport in a nanochannel. *Sci. in China Series E: Techn. Sci.* **2008,** *51* (7), 921-931.

27. Li, Y.; Xu, J.; Li, D., Molecular dynamics simulation of nanoscale liquid flows. *Micro. and Nanoflu.* **2010,** *9* (6), 1011-1031.

28. Shastry, B. S., Pharmacogenetics and the concept of individualized medicine. *Pharmacogenomics J* **2005,** *6* (1), 16-21.

29. Gilbert, W., DNA sequencing and gene structure Nobel lecture, 8 December 1980. *Biosci. reports* **1981,** *1* (5), 353-75.

30. Maxam, A. M.; Gilbert, W., New method for sequencing DNA. *PNAS* **1977,** *74* (2), 560-564.

31. Sanger, F., Determination of nucleotide-sequences in DNA. *Biosci. reports* **1981,** *1* (1), 3-18.

32. Sanger, F., Determination of Nucleotide-Sequences In DNA. *Science* **1981,** *214* (4526), 1205-1210.

33. Sanger, F., Determination of nucleotide sequences in DNA. *Biosci. reports* **2004,** *24* (4-5), 237-253.

34. Watson, J. D.; Crick, F. H. C., Molecular Structure of Nucleic Acids: A Structure for Deoxyribose Nucleic Acid. *Nature* **1953,** *171* (4356), 737-738.

35. (a) Venter, J. C.*et al*. The sequence of the human genome (vol 292, pg 1304, 2001). *Science* **2001,** *292* (5523), 1838-1838.

36. Tian, P.; Smith, G. D., Translocation of a polymer chain across a nanopore: A Brownian dynamics simulation study. *J. Chem. Phys.* **2003,** *119* (21), 11475-11483.

37. Meller, A.; Nivon, L.; Brandin, E.; Golovchenko, J.; Branton, D., Rapid nanopore discrimination between single polynucleotide molecules. *PNAS* **2000,** *97* (3), 1079-1084.

38. Kasianowicz, J. J.; Henrickson, S. E.; Weetall, H. H.; Robertson, B., Simultaneous multianalyte detection with a nanometer-scale pore. *Anal. Chem.* **2001,** *73* (10), 2268-2272.

39. Liang, X.; Chou, S. Y., Nanogap Detector Inside Nanofluidic Channel for Fast Real-Time Label-Free DNA Analysis. *Nano Lett.* **2008,** *8* (5), 1472-1476.

40. Pasternak, C. A.; Alder, G. M.; Apel, P. Y.; Bashford, C. L.; Korchev, Y. E.; Lev, A. A.; Rostovtseva, T. K.; Zhitariuk, N. I., Model pores for biological membranes: The properties of track-etched membranes. *Nuc. Instru. & Meth. in Phys. Res. Sect. B-Beam Interact. with Mat. and Atoms* **1995,** *105* (1-4), 332-334.

41. Han, J.; Turner, S. W.; Craighead, H. G., Entropic trapping and escape of long DNA molecules at submicron size constriction (vol 83, pg 1688, 1999). *Phys. Rev. lett.* **2001,** *86* (7), 1394-1394.

42. Martin, F.; Walczak, R.; Boiarski, A.; Cohen, M.; West, T.; Cosentino, C.; Ferrari, M., Tailoring width of microfabricated nanochannels to solute size can be used to control diffusion kinetics. *J. Contr. Release* **2005,** *102* (1), 123-133.

43. Lu, Z. X.; Namboodiri, A.; Collinson, M. M., Self-supporting nanopore membranes with controlled pore size and shape. *ACS Nano* **2008,** *2* (5), 993-999.

44. Turner, S. W.; Cabodi, M.; Craighead, H. G., Confinement-induced entropic recoil of single DNA molecules in a nanofluidic structure. *Phys. Rev. lett.* **2002,** *88* (12), 128103.

45. Danelon, C.; Santschi, C.; Brugger, J.; Vogel, H., Fabrication and Functionalization of Nanochannels by Electron-Beam-Induced Silicon Oxide Deposition†. *Langmuir* **2006,** *22* (25), 10711-10715.

46. Mao, P.; Han, J., Fabrication and characterization of 20 nm planar nanofluidic channels by glass-glass and glass-silicon bonding. *Lab on a Chip* **2005,** *5* (8), 837-844.

47. Steinmann, P.; Weaver, J. M. R., Fabrication of sub-5 nm gaps between metallic electrodes using conventional lithographic techniques. *J. Vac. Sci. & Techn.* **2004,** *22* (6), 3178-3181.

48. Menard, L. D.; Ramsey, J. M., Fabrication of Sub-5 nm Nanochannels in Insulating Substrates Using Focused Ion Beam Milling. *Nano Lett.* **2010**, null-null.

49. Kasianowicz, J. J.; Brandin, E.; Branton, D.; Deamer, D. W., Characterization of individual polynucleotide molecules using a membrane channel. *PNAS* **1996,** *93* (24), 13770-13773.

50. Li, T.; Hu, W. P.; Zhu, D. B., Nanogap Electrodes. *Adv. Mat.* **2010,** *22* (2), 286-300.

51. Chen, X.; Guo, Z.; Yang, G. M.; Li, J.; Li, M. Q.; Liu, J. H.; Huang, X. J., Electrical nanogap devices for biosensing. *Mat. Today* **2010,** *13* (11), 28-41.

CHAPTER 2. THEORY

2.1 Nanogap Detectors

Nanogap detectors are label-free biosensors consisting of two electron-conducting electrodes separated by an insulating gap of nanometer dimension. These detectors transduce biomolecules into useful electrical signals, generated from such properties as conductance, resistance, capacitance and/or impedance. Nanogaps are able to detect biomolecules by either observing their inherent electrical behaviors or monitoring changes in electrical behaviors of the medium within the detection volume when the biomolecules occupy the nanogap volume. Due to the inherent superiorities of electrical transduction methods, such as excellent compatibility with advanced semiconductor technology, better compatibility with scaling issues, and low cost, nanogap detectors are capable of detecting even single-molecules using simple instrumentation.

Electrical nanogaps can be either vertical or planar depending on the orientation of the electrodes relative to the substrate.[1] Vertical nanogaps have electrodes facing each other in the vertical direction with respect to the device plane while the electrodes in a planar nanogap configuration face each other horizontally with respect to the device plane.

Planar nanogap detectors can sense biomolecules either by trapping them within the nanogap, forming molecular junctions and observing their electrical behaviors (*e.g.* resistance, impedance, capacitance, quantum mechanical tunneling *etc.*) or by monitoring changes in the electrical conductance of the electrolyte within the detection volume when biomolecules occupy and displace ions of the electrolyte. In the former,

the biomolecule must be in contact with the electrodes. This is similar to the device described by Kawai *et al.*[2] However, in the latter, the biomolecule need not be in contact with the electrodes. Figure 2.1A shows the schematic of a planar nanogap detector.

The concept behind sensing based on volume exclusion is described in Figure 2.1B. When a biomolecule (charged or uncharged) of a characteristic conductivity arrives at the nanogap, it displaces buffer ions from the bulk electrolyte medium. The volume of buffer ions displaced approximately equals the 3-dimensional volume of the biomolecule. This volume exclusion causes a change in the concentration of buffer ions present in the nanogap with a corresponding change in the bulk conductivity of buffer ions within the nanogap. This is different from the concept of blockage currents used in nanopore sensing, in which case the detector only monitors the blockage in the ion-flux produced when biomolecules hinder buffer ions from traversing a region defined by the pore.

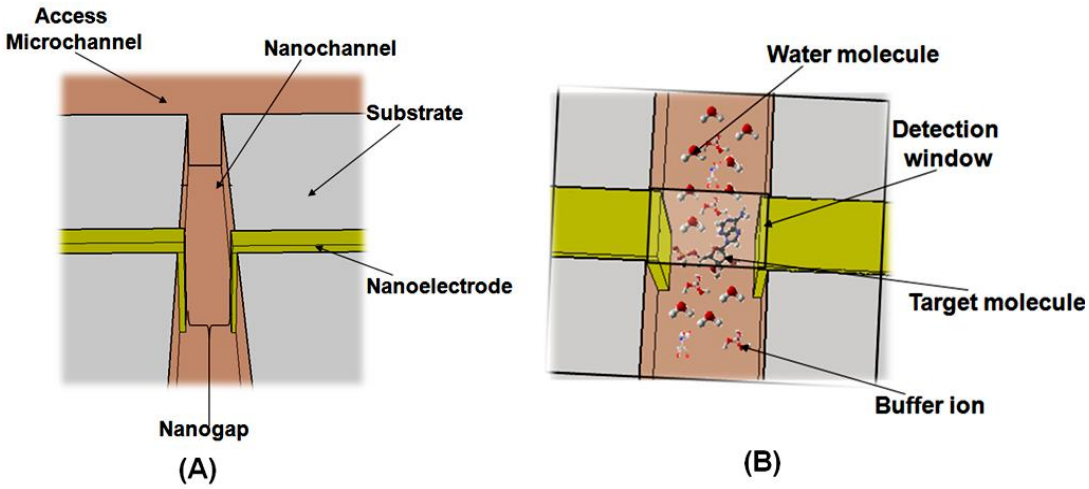

Figure 2.1(A) side view of a simple planar nanogap detector (B) top view of the planar nanogap detector describing the concept of bio-molecular sensing based on conductance changes due to volume exclusion.

Recently, horizontal nanogap detectors have been poised perpendicularly to nanochannels. The nanochannels terminate into microchannels at both ends. The microchannels allow easy filling of the nanochannels while the nanochannel helps in confinement. Liang *et al*.[3] reported the fabrication and characterization of a pair of planar nanogap detectors poised transversely to a nanochannel. The detector sensed electrokinetically driven dsDNA molecules traveling through the nanochannel. The principle was based upon monitoring the perturbation in the current caused by volume exclusion of 0.5X (pH 7.5) TBE buffer ions when the DNA was present in the nanogap.

For a detailed understanding of the transport mechanisms of DNA molecules through these integrated devices, in this chapter, we will briefly introduce some concepts of nanofluidics. Next, we will discuss electrokinetics, DNA confinement and the contribution of ions in confinement. Finally, we will describe DNA as a model for nanogap measurements and show representative equations in nanogap measurements.

2.2 Concepts in Nanofluidics

2.2.1 Electric Double Layer (EDL)

When a solid surface comes in contact with an aqueous solution comprised of an electrolyte, the solid surface becomes charged either due to the difference of electron (or ion) affinities between the solid surface and the solution or the ionization of surface groups.

For a glass surface immersed in an electrolyte and in immediate contact with an electrolyte, the glass surface acquires negative charges at a pH > 7. A layer of cations from the electrolyte therefore strongly binds to the solid surface. Outside this layer, another layer of mobile cations is generated as well. These two layers form a single

shielding layer usually referred to as the EDL or Debye Layer. Typically, the Gouy-Chapman-Stern model (GCS) is used to describe the EDL.[4]

As shown in Figure 2.2, the GCS model consists of two layers, which are the Stern layer (SL) and diffuse layer (DL). The SL is the region next to the solid surface and ions in the SL are bound near the surface due to adsorption and Coulomb interactions. The DL is the region next to the SL.

The thickness of EDL is an important electrokinetic parameter, especially in the field of nanofluidics. This is characterized by the Debye length, λ_d, and is represented in equation 1;

$$\lambda_d = \frac{\sqrt{\varepsilon_e R T}}{F\left(\sum_i z_i^2 c_i\right)^{\frac{1}{2}}} \qquad (1)$$

where the ionic strength of the electrolyte is represented as $I = \sum_i z_i^2 c_i$.[1] The ratio of EDL thickness to channel height h is used to describe the state of electroneutrality of the bulk solution within the channel. For channels with heights of several micrometers to >100 nm, it applies that $\frac{\lambda_D}{h} \ll 1$. In this case, the fluid away from the EDL and towards the center of the channel is electrically neutral *i.e.,* equal concentration of co-ions and counter-ions within the channel; see Figure 2.3A. In this case, the electric potential is also neutral. However, in cases where the channel height is on the order of the EDL thickness, that is $\frac{\lambda_D}{h} = 1$, there can be EDL overlap. This leads to an excess of counter-ions in the channel and loss of electroneutrality (Figure 2.3B).

2.2.2 Zeta Potential (or Electrokinetic Potential)

It is common that most surfaces submerged in an aqueous solution gain a net

charge density, which may originate from certain reaction equilibria like protonation, deprotonation, adsorption or defects in crystalline structure. Surface charges can also stem from external electric fields. For a monovalent electrolyte, λ_d is in the range of 0.1-100 nm for a concentration ranging from 10 to 0.01 mM.[5]

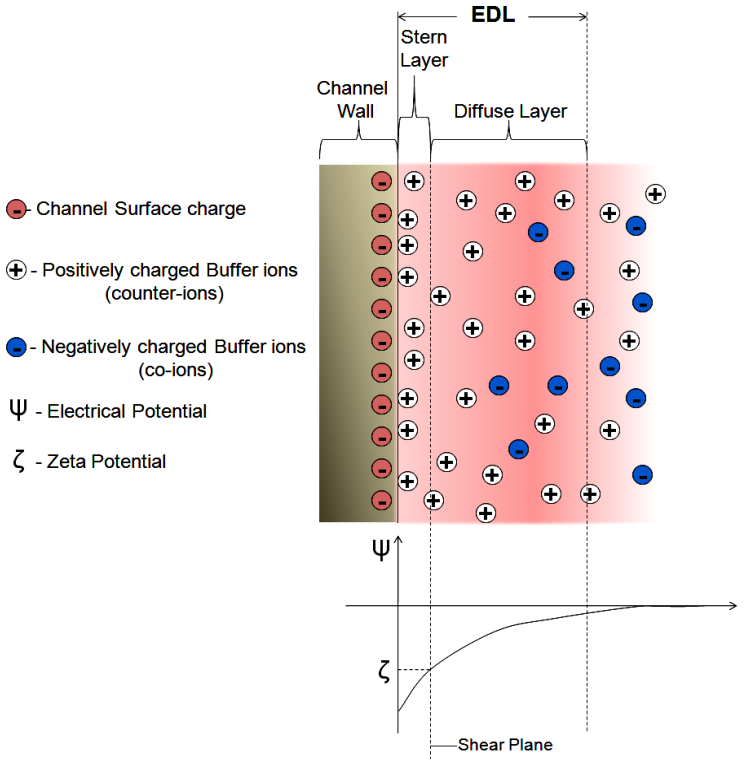

Figure 2.2 Model of the Electric Double layer at a Solid-liquid interface at a negatively charged solid surface/channel wall. Reproduced from reference [5] with Permission.

The zeta potential ζ is simply defined as a measure of the electric charge developed when a solid surface is brought into contact with an aqueous solution. It is the electrostatic potential at the boundary dividing the SL and DL. This boundary is known as the shear plane (see Figure 2.3). Therefore, the ζ-potential is the electric potential at the shear plane of the EDL. Typically, the values of ζ can vary between -200 mV to +200 mV depending on the chemistry of the solid/liquid interface. It is a property

that depends on the ion concentration, ion valency and size, pH and temperature of the solution.[6]

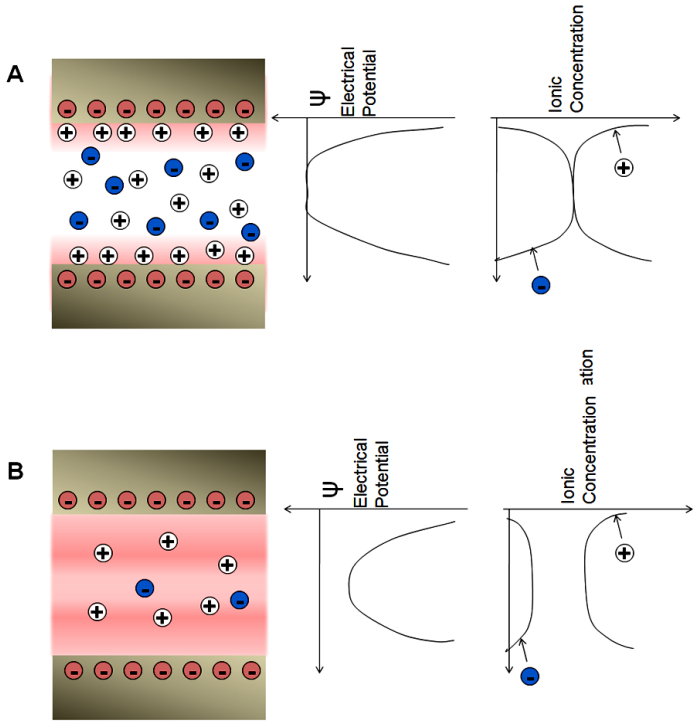

Figure 2.3 Illustration of differences in the electric potential and ionic concentrations for (A) Channels filled with moderately to highly concentrated electrolyte (and/or large channel height [h > λD]) and (B) Channels filled with low concentrated electrolyte (and/or small channel height [h ≤ λ_D]). Reproduced from reference [5] with Permission.

As a consequence, each solid-liquid interface will have its own unique zeta potential that must be measured. Sze *et al*.[7] reported that the ζ-potential for surfaces in KCl and $LaCl_3$ aqueous solutions varies in the range of -88 to -66 mV and -110 to -68 mV for glass and PDMS surfaces, respectively. These values were independent of the channel size and applied driving voltage.

The ζ-potential has been an important parameter in a number of microfluidic based applications[8,9] and in the characterization of membrane efficiency,[10] biomedical polymers[11,12] and electrokinetic transport of particles and blood cells.[13] The importance

of this value in a number of examples has led to a number of techniques developed for measuring this parameter. Measurements have been based on indirect readings using electrokinetic phenomena.[14,15,16] The Smoluchowski equation[7] (see equation 2) has been useful in computing the magnitude of the ζ-potential. It expresses the electroosmotic mobility, μ_{eof}, of a particle under the influence of an electric field in terms of the ζ-potential;

$$\mu_{eof} = 4\ \pi\ \varepsilon_0\ \varepsilon_r\ \frac{\zeta}{6\pi\eta}\ (1 + \kappa_d\ r) \qquad (2)$$

where κ_d is the Debye-Hückel parameter; $\kappa_d = \left(\frac{2\ C_i\ z_i^2\ q^2}{\varepsilon_r\ \varepsilon_0\ k_B\ T}\right)^{1/2}$

2.2.3 Electrical Conductivity

The electrical conductivity of a material (also known as specific conductance**,** κ (Sm^{-1}) is a measure of the ability of the material to conduct electrical current and represents the reciprocal of the resistivity ρ (Ωm) of the material. Electrical conductivity in a fluid is usually a product of the electrically-driven motion of ions under the influence of an external electric field.

The bulk conductivity, κ_b, of an electrolytic solution confined in a fluidic channel represents the electrical conductivity resulting from the motion of ions present in the bulk phase (toward the center of the channel and away from the EDL) under the influence of an electric field. As shown in equation 3, κ_b can be computed using Faraday's constant, (F = 96,485 C/mol), the effective ionic mobility u_i of the ions present and the ionic concentration c_i, in solution.[17, 18]

$$\kappa_b = F \sum_{Iil} |z_i|\ u_i\ c_i \qquad (3)$$

It is noteworthy that u_i is independent of the ionic concentration.[18] Michov[19] pointed out that at a specific concentration, u_i can be related to the absolute ionic mobility, u_i^{∞} as shown in equation 4 ;

$$u_i = \frac{u_i^{\infty}}{1 + \kappa_b r} \qquad (4)$$

where; $u_i^{\infty} = |z_i|\, q / 6\, \pi\, \eta\, r_i$

$$\therefore u_i = u_i^{\infty} - \frac{\kappa_b\, z_i\, q}{3\, \pi\, \eta} \qquad (5)$$

The bulk conductivity of a solution is also defined as the product of the total ionic concentration of ions in a solution and the molar conductivity.

$$\kappa_b = C_i \cdot \Lambda \qquad (6)$$

where; $\Lambda = z_+\, \lambda_+ + z_-\, \lambda_-$

The molar conductivity of a dissociable solute increases with ionization and thus depends on the concentration and pH; it decreases also by any interaction with other solutes and surfaces.[20]

The surface conductivity, κ_s, is regarded as an additional component to the electrical conductivity of fluids tangential to the charged surface and originating from excess counter-ions in the EDL region. Ions from the electrolyte are attracted towards the wall by electrostatic forces induced by the surface charge. Higher concentrations of ions towards the wall lead to a high surface conductivity. In many fluidic-based applications, κ_s is typically neglected. This is reasonable for most high concentration solutions with a low net charge density in the EDL region (thin EDL) or in microfluidic devices (large h). However, this is very likely to cause significant error for low concentration solutions. A more detailed description of κ_s has been reported by Lyklema

et al.[4, 21] Although it is possible that the motion of ions in the SL and DL contributes to the surface conductivity, the contribution of the less mobile SL is smaller compared to the more mobile DL. Actually, the SL contribution is sometimes called additional surface conductivity.

The surface conductivity, just as well as the zeta potential, is a very important interfacial electrokinetic property relevant to a number of natural phenomena, such as electrode kinetics, electrocatalysis, corrosion, adsorption, crystal growth, colloid stability and flow characteristics of colloidal suspensions and electrolyte solutions through porous media and microchannels. It is therefore important to measure κ_s in studies of electrokinetic phenomena. Specific surface conductivity values reported for water in glass capillaries is on the order of $10^{-9} \sim 10^{-8}\ \Omega^{-1}m^{-1}$.[22] Researchers have successfully determined the magnitude of the surface conductivity for other important materials.[23, 24, 25, 26] Bikerman[27] was the first to lay down a theoretical prediction for computing the surface conductivity. Squires *et al.*[28] reported the mathematical representation as shown in equation 7.

$$\kappa_s = 4\,\kappa_b\,\lambda_d\,(1 + m)\,\mathrm{Sinh}^2\left(\frac{z_i\,q_i\,\zeta}{4\,k_B T}\right) \qquad (7)$$

where; $m = \left(\frac{k_B T}{z_i\,q_i}\right)^2 \frac{2\,\varepsilon_w}{\eta\,D_u}$; $\varepsilon_w \approx 80\,\varepsilon_0$ and $D_u = \frac{\kappa_s}{\kappa_b\,a}$

The parameter *m* characterizes the contribution of electro-osmosis to the motion of ions within the DL.

2.2.4 Electroosmotic Flow (EOF)

The EOF was first reported by Reuss[29] in 1809. He showed that water could be made to percolate through porous clay diaphragms by the application of an external

electric field. The mobility of water was due to the fact that clay particles acquire a surface charge when in contact with an electrolyte that results in the formation of the EDL that induces a bulk flow of water ions. When an external electric field is applied across a capillary or channel containing ions (counter and co-ions), there is bulk movement of these ions from one electrode to the other. The positive ions (counter) in solution are attracted towards the cathode while the negative ions (co-ions) are attracted towards the anode; however, there is an excess of counter ions in the diffuse layer of the EDL. The movement of the excess counter ions will result in a viscous drag of the surrounding liquid molecules. This phenomenon results in a bulk flow of ions induced by the external electric field. This is referred to as the electroosmotic flow (EOF) and is illustrated in Figure 2.4A.

For a thin EDL or large channel height, the EOF has a 'Plug-like' (or flat) profile, unlike the typical hydrodynamic flow, which has a 'parabolic' profile (Figure 2.4B), This flat profile has been reported to result in high-efficiency electrokinetic separations.[30,31,32] The direction of the EOF depends upon the type of charge (positive or negative) on the channel wall.

For a negatively charged wall (as shown in Figure 2.4), under the influence of an external field, the EOF is towards the cathode while the direction of the EOF is reversed for a positively charged wall. The mathematical representation of the EOF velocity, v_{eof}, shown in equation 8 is generated by combining Newton's Law applied to viscous fluids and Poisson's charge distribution.

$$v_{eof} = - \frac{\varepsilon_r E \zeta}{\eta} \qquad (8)$$

Because the EOF mobility is the ratio of the EOF velocity and the applied field strength (*i.e.* $\mu_{eof} = \frac{v_{eof}}{E}$),

$$\mu_{eof} = -\frac{\varepsilon \zeta}{\eta} \qquad (9)$$

It can be deduced from equation 9 that μ_{eof} depends on channel wall conditions, properties of the solution (viscosity and ionic strength), pH and composition of the background electrolyte. Typically, parameters that influence the charge on the channel wall will greatly influence the zeta potential and EOF mobility.

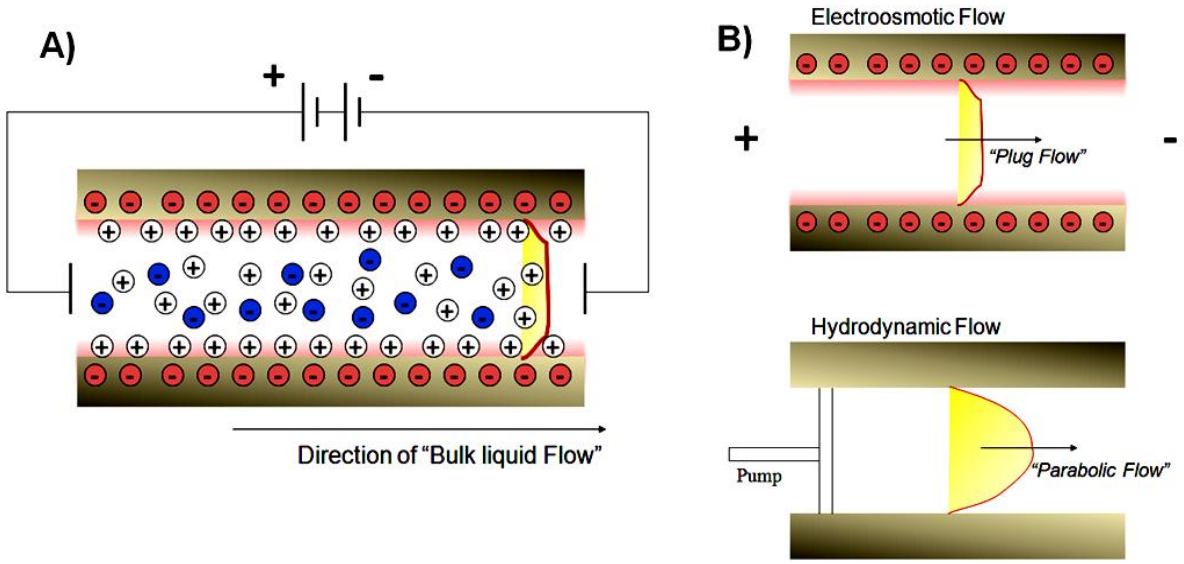

Figure 2.4(A) 'Plug-like' flow profile of EOF for negatively charged channel under the influence of an external electric field (B) Comparison between the shapes of the plug flow (electric field driven) and hydrodynamic (pressure driven) flow.

2.2.5 Electrophoresis

Electrophoresis is the transport of charged colloidal particles or poly-electrolytes relative to the stationary bulk liquid under the influence of an external electric field. Because most species in micro- and nanofluidics are charged, electrophoresis provides a convenient method of transporting these species in fluidic devices. Among the most

important examples are biomolecules, such as proteins and DNA and colloidal particles, such as latex spheres. Successful separations of these particles by their zeta potential or size have been extensively reported.[33] Electrophoresis requires that the fluids entraining these particles are able to conduct electricity. In most cases, these solutions contain salts that dissociate into cations and anions. For dilute solutions containing simple ions that do not interact electrostatically when placed in a uniform electric field, E, (generated when a potential, V, is applied between two electrodes separated by a distance, L; $E = \frac{V}{L}$).

The electrophoretic velocity, v_{ep}, relates linearly to the electric field strength and the electrophoretic mobility, μ_{ep};

$$v_{ep} = \mu_{ep} E \qquad (10)$$

The electric force acting on the ions in solution is the product of its charge, q_i, and the electric field. ($q_i > 0$ for cations and $q_i < 0$ for anions).

$$F_e = q_i \cdot E \qquad (11)$$

If the ion is approximated as a spherical particle with a geometrical radius, r_i and migrating through a fluid of viscosity, η, then the drag coefficient, ξ (Stokes drag) and the drag force, F_d, are given by the equations;

$$\xi = 6 \pi \eta r_i \quad ; \quad F_d = - \xi v_{ep} \qquad (12)$$

2.2.6 Electrical Noise

The most significant forms of noise associated with high bandwidth electrical measurements involving single molecules across nano-scale electrodes are shot noise and Johnson-Nyquist noise. Shot noise, I_{noise} (rms) or I_{ns}, is manifested as direct current fluctuations due to the discreteness of electrical charge (equation 13) while Johnson

noise, I_{noise} (rms) or I_{nj}, is a result of fluctuations in voltage across a conductor in thermal equilibrium and can be modeled by a current source in parallel with the resistor as shown in equation 14.

$$I_{ns} = [\, 2\, q\, I_{dc}\, B]^{1/2} \qquad (13)$$

$$I_{nj} = \left[\frac{4\ k_B\, T\, B}{R} \right]^{1/2} \qquad (14)$$

The total 'rms' noise contributions to the current from different sources can be calculated using;

$$I_{total}(rms) = \sqrt{\left(I_a^2 + I_b^2 + \ldots\ldots\ldots\ldots I_n^2 \right)}\ ; \qquad I_{rms} = \frac{I_{DC}}{\sqrt{2}} \qquad (15)$$

2.3 Electrokinetic Flows

Electrokinetic phenomena involve tangential fluid motion adjacent to a charged surface. They offer several advantages that include short processing time, high-resolution and low-cost analysis. Electrokinetic phenomena are manifestations of the electrical properties of interfaces under steady state and isothermal conditions and have been developed in close connection with the theories of the EDL and of electrostatic surface forces. As dimensions are reduced from the macroscopic scale to the nano-scale for fluid/particle transport, there are changes in the dominating forces as well as the physics of the transport process. These changes, as reported by Gad-el Hak,[34] are due to an increase in the surface-to-volume ratio as the dimensions are scaled down. As a consequence, forces resulting from pressure, inertia, viscosity or gravity that usually plays the dominant role in macroscopic flows may not be practical in micro/nanofluidic systems while interfacial forces, like surface tension, become immensely dominant. To move materials, such as water, ions and particles, in these

reduced-scale systems, especially nanoscale devices, pressure driven flow becomes very difficult and sometimes impossible; hence, electrokinetic (EK) transport becomes a more convenient approach. In 2005, Conlisk[1] in his work provided a graphical representation showing the pressure drop (Δp) and applied voltage (V) as a function of channel height (Figure 2.5).

From the graphical representation shown in Figure 2.5, it can be deduced that as the height of the channel is reduced to 10 nm for a flow-rate of 1 µl/min, the pressure drop increases from 0.006 to 3 atmospheres, while the corresponding voltage drop changes from 0.05 V to 0.33 V. The pressure drop reveals a large drop and clearly, a relatively awkward pump would be required to deliver this modest flow rate at such a high pressure drop. However, the magnitude of the voltage drop makes the electrokinetic driven flow more practical.

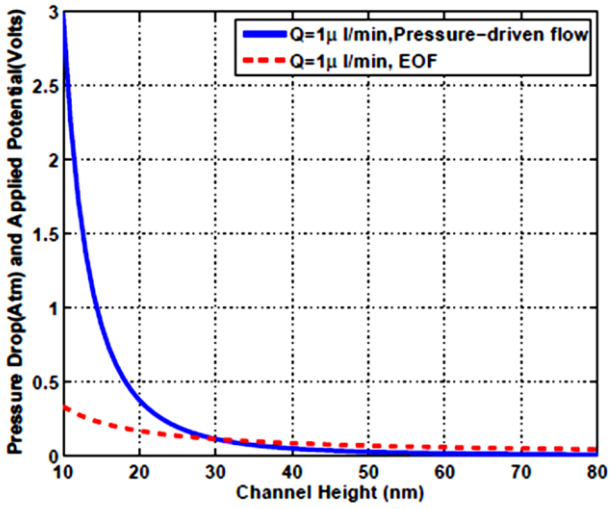

Figure 2.5 Required pressure drop and voltage drop for nanochannels with different channel heights. Nanochannel length and width are 3.5 µm and 2.3 µm, respectively, zeta potential is -11 mV, electrolyte is 1M NaCl.

2.4 Confinement and Stretching of DNA in Nanochannels

In designing chip-based analysis systems for studies of dsDNA, it is crucial to

understand the behavior of dsDNA in confined geometries. Recently, it has been reported that a DNA molecule in a nanochannel will stretch along the channel axis to a substantial fraction of its full contour length.[35] Confinement elongation of genomic-length DNA has several advantages over alternative techniques for extending DNA, such as flow stretching and/or stretching relying on a tethered molecule. Confinement elongation does not require the presence of a known external force because a molecule in a nanochannel will remain stretched in its equilibrium configuration and hence, the mechanism is in equilibrium. It also allows for continuous measurement of length.[36] In confined spaces, where R_G is much larger than the nanochannel width D, the number of available configurations for the polymer chain is reduced. Two confinement regimes exist and depend on differences between the channel width D and persistence length l_p.

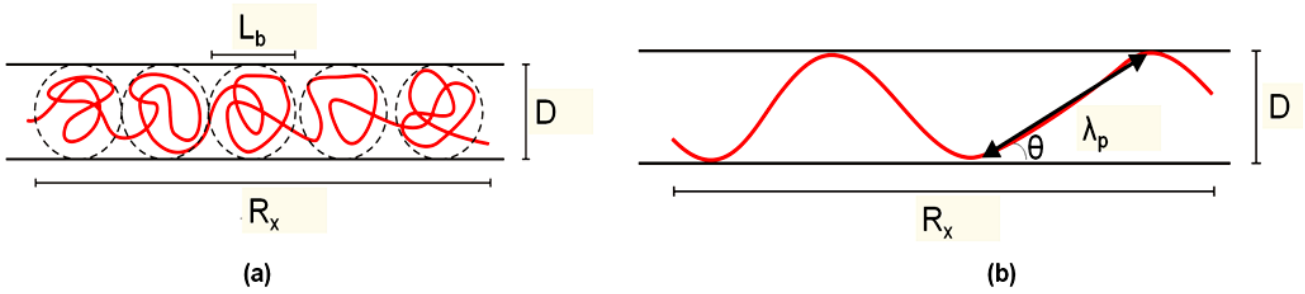

Figure 2.6 (a) deGennes regime and (b) Odijk regime in DNA confinement.

When D >> l_p, the molecule is free to coil within the nanochannel and stretching is entirely due to excluded volume interactions between different coiled segments of the polymer separated along the backbone. Coiling of the molecule can be envisioned to be broken up in a series of blobs with diameter L_b, while the stretching is a result of repulsion between the blobs. This is known as the de Gennes regime.[37] Within the blobs, the confinement force is only a weak perturbation while each blob retains the

property of the bulk polymer. This is diagrammatically illustrated in Figure 2.6a. The extension of the molecule, R_x, can be calculated using equation 16;

$$R_x = L_{cont} \left(\frac{w_{eff}\ l_p}{D_{av}^2} \right)^{1/3} \qquad (16)$$

where $D_{av} = \sqrt{D \times h}$ and is the geometrical average of the two confining dimensions in the nanochannels.

As the channel width drops and $D << l_p$, the stretching is strictly not a result of volume exclusion but an interplay between confinement and the intrinsic elasticity of the DNA. The strong confinement prevents the molecule from forming loops within the nanochannel. Back folding becomes energetically unfavorable and stretching becomes a result of deflection of the molecules in the channel walls. The average length between these deflections is of the order of the Odijk length scale $\lambda_p \cong (D_{av}^2\ l_p)^{1/3}$. This regime is referred to as the Odijk regime, Figure 2.6b.[38, 39] For a small average deflection, θ, R_x is represented as;

$$R_x = L_{cont} \cos\theta \cong L_{cont} \left[1 - 0.23 \left(\frac{D_{av}}{l_p} \right)^{2/3} \right] \qquad (17)$$

2.5 Effects of Changes in Ionic Environment on DNA Molecules

According to Reisner *et al.*[35] ionic strength variations affect the polymer configuration by modulating the range of electrostatic interactions between charges on the DNA phosphate backbone. Electrostatic interactions in electrolyte solution are screened over a characteristic scale known as the Debye length. The geometry of the polymer results in two types of electrostatic interactions;[36]

- Interactions between charges separated in contours that create repulsion between back looping segments. This has been reported to be the reason for creating an effective DNA width (w_{eff}) larger than the intrinsic width w_o.
- Local repulsive interactions between charges separated by less than the Debye length in contour resulting in an increase in the persistence length to a new value for l_p.

The mechanisms of these interactions determine the ionic strength variation of the extension over an ionic strength range. The Odijk-Skolnick-Fixman[40] equation based on single-molecule elasticity has suggested that the new persistence length of a DNA when in solution is related to the ionic strength of the solution by;

$$l_p = l_{p_o} + \frac{0.0324\ \text{M}}{\text{I}}\ \text{nm} \qquad (18)$$

where l_{p_o} = high salt value of persistence length (= 50 nm).

According to equation 18, l_p is roughly equal to l_{p_o} until the ionic strength drops below 10 mM. It can rise up to about 80 nm between 10 mM and 1 mM. Although, reports have shown that the extension of DNA along a nanochannel almost triples over two decades' variation in ionic strength, the extension variation cannot, however, be explained by the ionic strength dependence of the persistence length alone. This is in contrary to a report by Krishnan *et al*.[41] Reisner *et al*. reported, based on their experiment, that even over a range of 4 - 200 mM ionic strength, variation in the persistence length was not large enough to explain the observed extension of DNA. This is why an additional mechanism, which involves confining the DNA in a nano-confined environment, is required.

2.6 DNA as a Model Polymer for Nanogap Measurements

When dealing with long molecules, and their associated number of degrees of freedom, it is useful to treat the behavior of this polymer by statistical quantities. The mean-square end-to-end distance (or displacement length) R_F^2 and the mean-square radius of gyration, R_G^2 are two important quantities in conformational statistics of the polymer chains that provide information about on the actual size of a polymer. A polymer chain will take up a finite volume of space, and thus the monomers will occupy an excluded volume around themselves. Other monomers are not allowed to enter this excluded volume due to steric hinderance, repulsive effects and interactions with the solvent.

Although, the biological properties of a DNA molecule are very complex, the physical properties involved in the molecular dynamics can be described by three parameters; the contour length, L_{cont}, persistence length, l_p and the effective width, w_{eff}.[42] The contour length refers to the total length of the DNA when it is fully stretched. As stated by Watson and Crick, each base pair contributes 0.34 nm to the full contour length. Due to its double helical structure, the DNA molecule becomes locally rigid.[43]

Persistence length for DNA have been extensively evaluated and reported by Hays *et al*.[44] from light-scattering measurements of the molecular weight and the mean-square radius and with the aid of hydrodynamic theory measurements of intrinsic viscosity and the sedimentation coefficient. On length scales smaller than l_p, a DNA molecule can be considered rigid, while the molecule is flexible on length scales larger than l_p. An intrinsic persistence length of ~50 nm (150 bp) in 0.1 M aqueous NaCl has been reported for dsDNA molecules.[45] The intrinsic width (w_0) of dsDNA is 2 nm. The

effect of self-avoidance on flexible polymers that are freely coiled in solution was first understood by Flory[46, 47] and later generalized to the semi-flexible case by Schaefer *et al*.[48] Flory-Pincus represented the R_F for a real polymer by the equation below;

$$R_F \cong (l_p \ w_{eff})^{1/5} L_{cont}^{3/5} \qquad (19)$$

The radius of gyration was related to R_F by;

$$R_G \cong \frac{R_F}{\sqrt{6}} \qquad (20)$$

We can calculate the bulk R_G for DNA molecules that will be subsequently used in this experiment. Based on the values reported by Reisner *et al.*,[35] for 0.5X TBE buffer with 20 mM ionic concentration, w_o = 2 nm, w_{eff} was estimated to be 12 nm. It has been reported that the intercalation of YOYO-1 dye to dsDNA causes an extension in the contour length by approximately the length of two base pairs (~0.68 nm). At a dye concentration, of 1 dye molecule per 5 base pairs, a 27% increase in the contour and persistence length is assumed. The adjusted persistence length will be 64 nm and the contour lengths of lambda (λ) and T4 DNA will be L_λ = 20.9 μm and L_{T4} = 71.5 μm. Therefore, based on equations 19 and 20, the radius of gyration for each DNA will be approximately 602 nm and 1260 nm for λ and T4 DNA, respectively.

Figure 2.7 presents representative equations for computing the signals from ion-flux blockage (see Figure 2.7A) and the signal from volume exclusion at a nanogap detector (see Figure 2.7B). In segment A, the longitudinal blockage current results when a DNA traveling through a nanochannel blocks the ion-flux through the nanochannel. In segment B, similar to the device by Liang *et al.,*[3] the transverse current resulting from volume exclusion at the detection window is monitored while segment C, similar to our

nanogap device, monitors the time taken for molecules to travel between electrodes1,2 (input electrodes) and electrodes 3,4 (output electrodes).

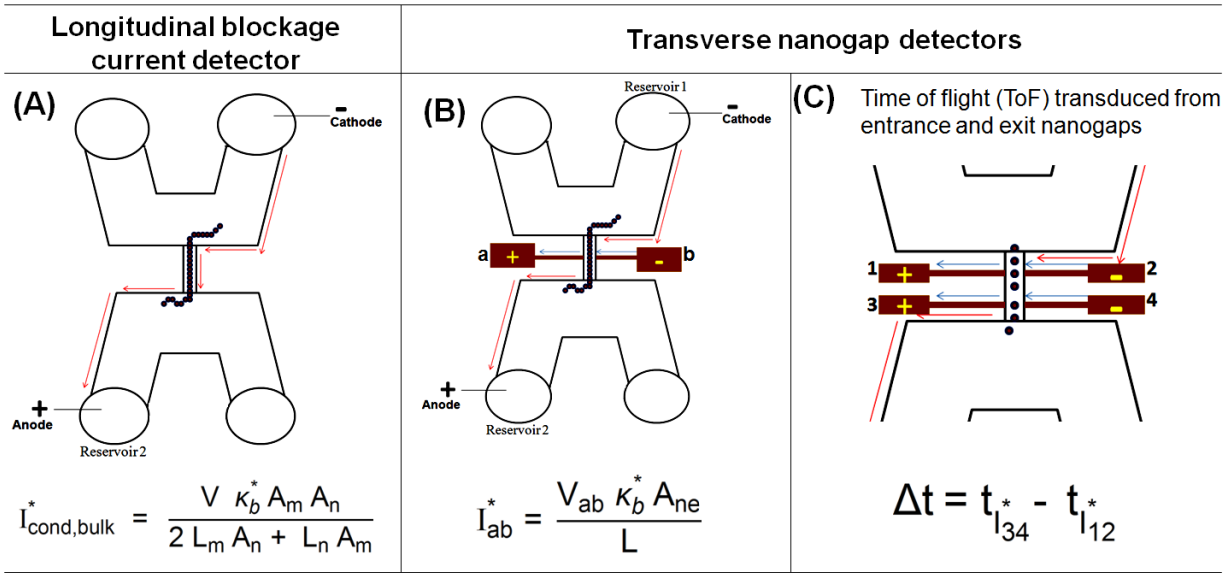

Notes;

Longitudinal Blockage current detector

$I^*_{cond,bulk}$ = Bulk longitudinal current in the presence of Biomolecules

$I_{cond,bulk}$ = Bulk longitudinal current in the absence of Biomolecules

$I_{cond,bulk} > I^*_{cond,bulk}$; *Signal* ($\Delta I = I_{cond,bulk} - I^*_{cond,bulk}$)

(Length of biomolecules varies directly as the duration of signal)

κ_b^* = Bulk conductance of the buffer ions in the presence of biomolecules

κ_b = Bulk conductance of the buffer ions in the absence of biomolecules

V = Voltage bias between cathode and anode *(along red arrows)*

Transverse nanogap detector

I^*_{ab} = Electric current across electrodes a and b in the presence of biomolecules

I_{ab} = Electric current across electrodes a and b in the absence of biomolecules

V_{ab} = Voltage bias across electrodes a & b *(along blue arrows)*

L = Nanogap size (Width of spacing between electrodes)

ToF (Δt) = Time of Flight (time duration between electric current observed across nanogaps 3 & 4 and 1 & 2)

Figure 2.7 Schematics and equations for computation of signals from longitudinal blockage current and transverse nanogap currents.

2.7 References

1. Li, T.; Hu, W. P.; Zhu, D. B., Nanogap Electrodes. *Adv. Mat.* **2010,** *22* (2), 286-300.
2. Tsutsui, M.; Taniguchi, M.; Yokota, K.; Kawai, T., Identifying single nucleotides by tunnelling current. *Nature Nano.* **2010,** *5* (4), 286-290.
3. Liang, X.; Chou, S. Y., Nanogap Detector Inside Nanofluidic Channel for Fast Real-Time Label-Free DNA Analysis. *Nano Lett.* **2008,** *8* (5), 1472-1476.

4. J.Lyklema, *Fundamentals of Interface and Colloid Science. Vol. 2 - Solid-Liquid Interfaces*. First Edition ed.; Academic Press: London, England, 1995; Vol. Volume 2.

5. Abgrall, P.; Nguyen, N. T., Nanofluidic Devices and Their Applications. *Anal. Chem.* **2008,** *80* (7), 2326-2341.

6. Kirby, B. J.; Hasselbrink, E. F., Zeta potential of microfluidic substrates: 1. Theory, experimental techniques, and effects on separations. *Electrophoresis* **2004,** *25* (2), 187-202.

7. Sze, A.; Erickson, D.; Ren, L. Q.; Li, D. Q., Zeta-potential measurement using the Smoluchowski equation and the slope of the current-time relationship in electroosmotic flow. *J. Colloid and Interf. Sci.* **2003,** *261* (2), 402-410.

8. Ross, D.; Gaitan, M.; Locascio, L. E., Temperature Measurement in Microfluidic Systems Using a Temperature-Dependent Fluorescent Dye. *Anal. Chem.* **2001,** *73* (17), 4117-4123.

9. Erickson, D.; Li, D., Analysis of Alternating Current Electroosmotic Flows in a Rectangular Microchannel. *Langmuir* **2003,** *19* (13), 5421-5430.

10. Reischl, M.; Stana-Kleinschek, K.; Ribitsch, V., Adsorption of surfactants on polymer surfaces investigated with a novel zeta-potential measurement system. In *Adv. Mat. Forum Iii, Pts 1 and 2*, Vilarinho, P. M., Ed. 2006; Vol. 514-516, pp 1374-1378.

11. Werner, C.; König, U.; Augsburg, A.; Arnhold, C.; Körber, H.; Zimmermann, R.; Jacobasch, H. J., Electrokinetic surface characterization of biomedical polymers - A survey. *Colloids and Surfaces A: Physicochem. and Eng. Aspects* **1999,** *159* (2-3), 519-529.

12. Werner, C.; Jacobasch, H. J., Surface characterization of polymers for medical devices. *Int. J. Art. Organs* **1999,** *22* (3), 160-176.

13. Minerick, A. R.; Ostafin, A. E.; Chang, H.-C., Electrokinetic transport of red blood cells in microcapillaries. *Electrophoresis* **2002,** *23* (14), 2165-2173.

14. Oddy, M. H.; Santiago, J. G., A method for determining electrophoretic and electroosmotic mobilities using AC and DC electric field particle displacements. *J. Colloid and Interf. Sci.* **2004,** *269* (1), 192-204.

15. Alkafeef, S. F.; Alajmi, A. F., Streaming potentials and conductivities of reservoir rock cores in aqueous and non-aqueous liquids. *Colloids and Surfaces A: Physicochem. and Eng. Aspects* **2006,** *289* (1-3), 141-148.

16. Werner, C.; Körber, H.; Zimmermann, R.; Dukhin, S.; Jacobasch, H.-J., Extended Electrokinetic Characterization of Flat Solid Surfaces. *J. Colloid and Interf. Sci.* **1998,** *208* (1), 329-346.

17. Bard, A. J., *Electrochemical Methods: Fundamentals and Applications*. Second ed.; Wiley New York, 2001; p 856.

18. Coury, L., Conductance Measurements Part 1: Theory. *Current Sep.* **1999,** *18* (3), 91-96.

19. Michov, B. M., Ionic Mobility Parameter. *Electrophoresis* **1985,** *6* (9), 471-474.

20. Brody, J. R.; Kern, S. E., History and principles of conductive media for standard DNA electrophoresis. *Anal. Biochem.* **2004,** *333* (1), 1-13.

21. Lyklema, J.; Minor, M., On surface conduction and its role in electrokinetics. *Colloids and Surfaces A: Physicochem. and Eng. Aspects* **1998,** *140* (1-3), 33-41.

22. Gu, Y.; Li, D., The [zeta]-Potential of Glass Surface in Contact with Aqueous Solutions. *J. Colloid and Interf. Sci.* **2000,** *226* (2), 328-339.

23. Alberghi.Je; Broudy, R. M., Surface Conductivity on degenerate Germanium. *Phys. Rev. Lett.* **1966,** *17* (16), 863-&.

24. Stec, K.; Szroeder, P.; Benzhour, K., High Temperature Surface Conductivity of Hydrogenated Diamond Films Exposed to Humid Air. *Acta Physica Polonica A* **2010,** *118* (3), 511-514.

25. Perevert.Vd; Zapkov, V. T., Nature of a surface conductivity for Mica. *Izvestiya Vysshikh Uchebnykh Zavedenii Fizika* **1972,** (8), 121-&.

26. Revil, A.; Glover, P. W. J., Nature of surface electrical conductivity in natural sands, sandstones, and clays. *Geophys. Res. Lett.* **1998,** *25* (5), 691-694.

27. Bikerman, J. J., Ionic theory of electroosmosis, the current flow and the surface conductivity. *Zeitschrift Fur Physikalische Chemie-Abteilung a-Chemische Thermodynamik Kinetik Elektrochemie Eigenschaftslehre* **1933,** *163* (5/6), 378-394.

28. Squires, T. M.; Bazant, M. Z., Induced-charge electro-osmosis. *J. Fluid Mech.* **2004,** *509*, 217-252.

29. F, R. F., *Memoires de la Societe Imperiale des Naturalsites de Moscou* **1809,** *2*, 327.

30. Jorgenson, J. W.; Lukacs, K. D., Zone electrophoresis in open-tubular Glass-Capillaries. *Anal. Chem.* **1981,** *53* (8), 1298-1302.

31. Rice, C. L.; Whitehead, R., Electrokinetic Flow in a Narrow Cylindrical Capillary. *J. Phys. Chem.* **1965,** *69* (11), 4017-4024.

32. Paul, P. H.; Garguilo, M. G.; Rakestraw, D. J., Imaging of Pressure- and Electrokinetically Driven Flows through Open Capillaries. *Anal. Chem.* **1998,** *70* (13), 2459-2467.

33. Viovy, J. L., Electrophoresis of DNA and other polyelectrolytes: Physical mechanisms. *Rev. of Mod. Phys.* **2000,** *72* (3), 813-872.

34. (a) Gad-el-Hak, M., The fluid mechanics of microdevices - The Freeman Scholar Lecture. *J. Fluids Eng.-Transactions of the Asme* **1999,** *121* (1), 5-33; (b) Conlisk,

A. T., The Debye-Huckel approximation: Its use in describing electroosmotic flow in micro- and nanochannels. *Electrophoresis* **2005,** *26* (10), 1896-1912.

35. Reisner, W.; Beech, J. P.; Larsen, N. B.; Flyvbjerg, H.; Kristensen, A.; Tegenfeldt, J. O., Nanoconfinement-enhanced conformational response of single DNA molecules to changes in ionic environment. *Phys. Rev. Lett.* **2007,** *99* (5).

36. Tegenfeldt, J. O.; Prinz, C.; Cao, H.; Chou, S.; Reisner, W. W.; Riehn, R.; Wang, Y. M.; Cox, E. C.; Sturm, J. C.; Silberzan, P.; Austin, R. H., The dynamics of genomic-length DNA molecules in 100-nm channels. *PNAS* **2004,** *101* (30), 10979-10983.

37. Chu, B., Scaling Concepts In Polymer Physics - Degennes,Pg. *J. Ame. Chem. Soc.* **1983,** *105* (15), 5169-5169.

38. Odijk, T., DNA confined in nanochannels: Hairpin tightening by entropic depletion. *J. Chem. Phys.* **2006,** *125* (20).

39. Odijk, T., ON THE STATISTICS AND DYNAMICS OF CONFINED OR ENTANGLED STIFF POLYMERS. *Macromolecules* **1983,** *16* (8), 1340-1344.

40. Baumann, C. G.; Smith, S. B.; Bloomfield, V. A.; Bustamante, C., Ionic effects on the elasticity of single DNA molecules. *PNAS* **1997,** *94* (12), 6185-6190.

41. Krishnan, M.; Mönch, I.; Schwille, P., Spontaneous Stretching of DNA in a Two-Dimensional Nanoslit. *Nano Lett.* **2007,** *7* (5), 1270-1275.

42. Reisner, W.; Morton, K. J.; Riehn, R.; Wang, Y. M.; Yu, Z.; Rosen, M.; Sturm, J. C.; Chou, S. Y.; Frey, E.; Austin, R. H., Statics and dynamics of single DNA molecules confined in nanochannels. *Phys. Rev. Lett.* **2005,** *94* (19), 196101.

43. Manning, G. S., Three persistence lengths for a stiff polymer with an application to DNA B-Z junctions. *Biopolymers* **1988,** *27* (10), 1529-1542.

44. Hays, J. B.; Magar, M. E.; Zimm, B. H., Persistence length of DNA. *Biopolymers* **1969,** *8* (4), 531-&.

45. Manning, G. S., The persistence length of DNA is reached from the persistence length of its null isomer through an internal electrostatic stretching force. *Biophysical Journal* **2006,** *91* (10), 3607-3616.

46. Orland, H., Flory Theory revisited. *Journal De Physique I* **1994,** *4* (1), 101-114.

47. Baumgärtner, A., Excluded volume effect on polymer films. *Polymer* **1982,** *23* (3), 334-335.

48. Schaefer, D. W.; Joanny, J. F.; Pincus, P., Dynamics of Semiflexible Polymers in Solution. *Macromolecules* **1980,** *13* (5), 1280-1289.

CHAPTER 3. FABRICATION OF NANOGAP DEVICE

In this chapter, the fabrication and electrical characterization of the integrated nanofluidic/nanogap device are described. The device was fabricated using lithography conditions in a class 100 clean room at Ulsan National Institute of Science and Technology, South Korea. Fused silica wafers (500 μm thick) with surface roughness of ~0.3 nm (RMS) was used as the substrate. The final dimensions of the assembled chip were 20 mm x 20 mm. Figure 3.1 shows a schematic of the integrated device.

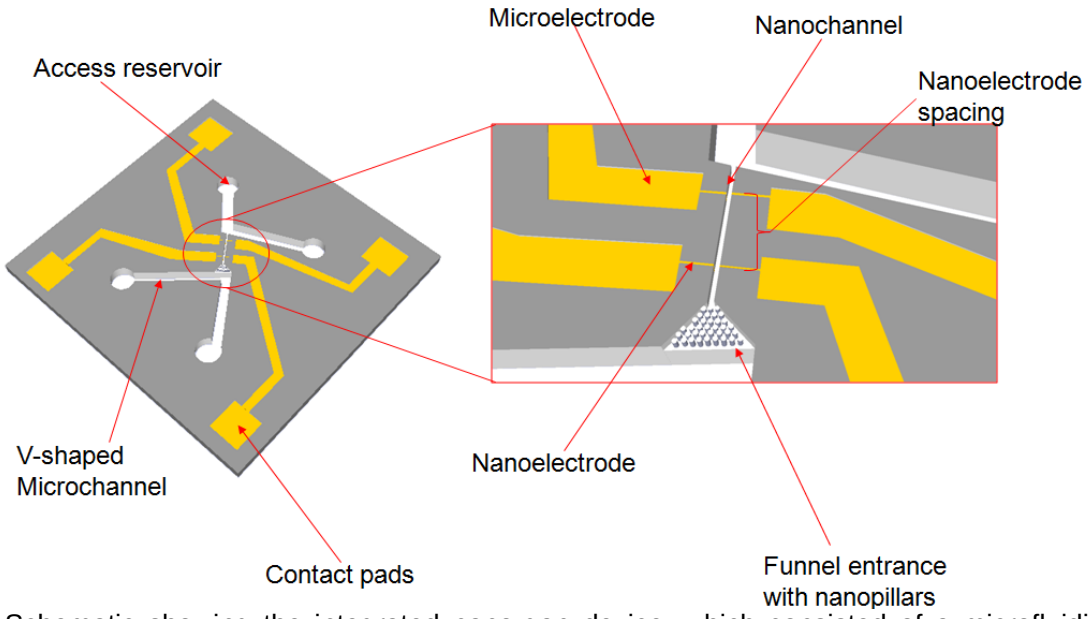

Figure 3.1 Schematic showing the integrated nano-gap device, which consisted of a microfluidic network, a nanochannel with input funnel, microelectrodes and two nano-electrodes that were poised at the input and output ends of the nanochannel.

The sequence of the fabrication steps was carefully selected after alternative schemes were deemed unsuccessful; the selected process resulted in the optimized strategy to make the desired structures. During the process pipeline development, it was important to make sure that a subsequent fabrication step(s) did not compromise the outcome of previous steps nor interfere with down-stream processing steps. The

entire protocol is summarized in Figure 3.2 with specific processing steps extensively described in subsequent sections of this chapter.

3.1 Device Design

In many micro- and nanofabrication processing strategies that require direct patterning of a substrate, the first step typically involves making alignment marks to provide the alignment of features made in each step of device fabrication. In our process strategy, an alignment mark, made from chrome metal, was patterned onto the fused silica substrate (not shown in the schematic). This was performed using standard UV-lithography followed by e-beam evaporation of 100 nm Cr layer and lift-off.

3.1.1 Microelectrodes and Contact Pads (Steps 1-2, see Scheme 3.1)

Fabrication of the device began with designing the microelectrodes and contact pads. This was done so as to eliminate problems that may arise from machining fluidic channels or access holes if done prior to this step. These problems could include, non uniform coating of the photoresist on the wafer, difficulty in patterning the electrodes positioned between the microchannels, possible misalignment of the wafer with respect to the optical mask, irregular deposition of the electrodes and non-uniform surfaces, which could impede bonding a cover plate to the substrate.

As shown in Scheme 3.1, fabricating the microelectrodes and contact pads involved the following steps: (1) Patterning trenches in a resist by optical lithography, (2) etching with ICP-reactive ion etching, and (3) electron-beam evaporation of the Au electrodes.

Before spin coating the photoresist on the substrate for optical lithography, the wafer was pretreated with hexamethyldisilazane (HMDS). HMDS is used to ensure

good adhesion between the photoresist and the quartz substrate and allows for easy removal of the resist after etching. The treated substrate was spin coated with a positive photoresist, AZ1512, on a spin coater running at 4000 rpm for 30 s. The resist thickness was ~1.5 μm. The coated wafer was aligned with a mask using the small Cr alignment marks before UV exposure. The alignment and exposure was performed with an MA6 Mask Aligner (SUSS MICROTEC) with 110 mJ/cm^2 UV energy. The microelectrode mask was designed with AutoCAD software and is shown in Figure 3.2A.

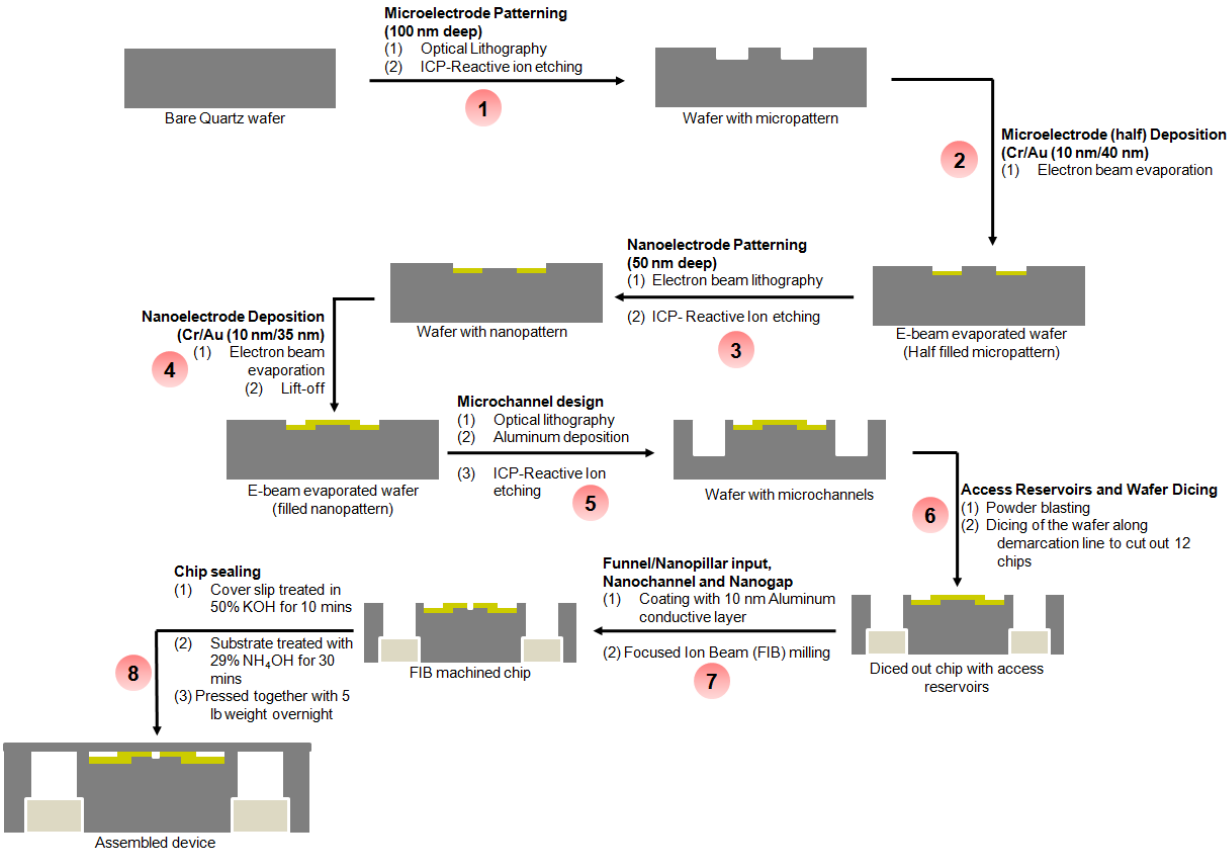

Scheme 3.1 Fabrication scheme for the nanogap device. Eight different processing steps were required and generally involved micro-patterning (optical lithography, e-beam evaporation, reactive ion etching) and nano-patterning (electron beam lithography, FIB and reactive ion etching).

Following exposure, the photoresist was baked at 105^{0}C for 1 min and developed in an AZ300MIF developing solution for 60 s. The developed wafer was then cleaned by flushing with deionized water followed by spin drying. A 100 nm Al layer was coated onto the wafer using a DC sputter coater running at 70 W and 10 mTorr. The Al metal layer served to prevent charging and broadening of structures during ICP-RIE.

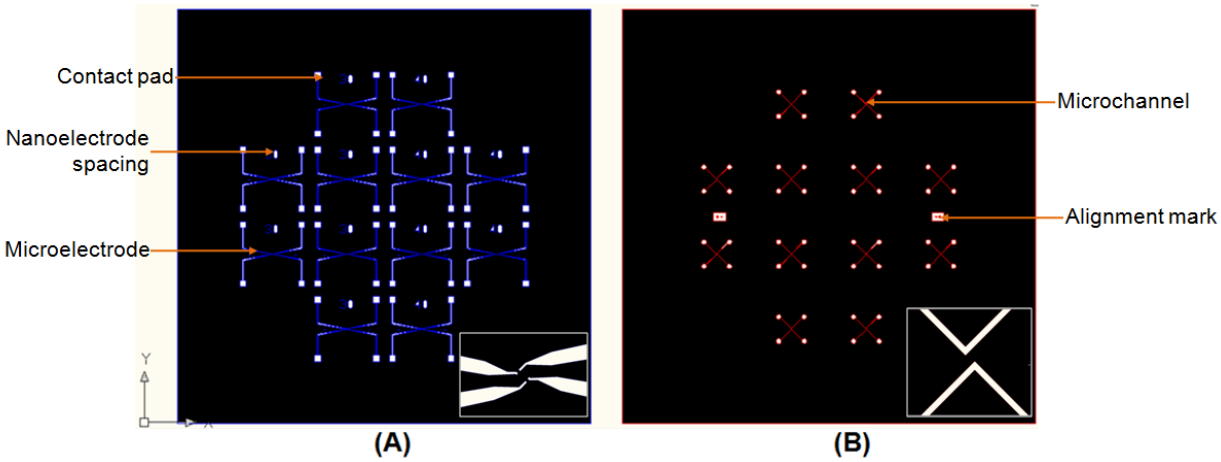

Figure 3.2 (A) Microelectrode mask (insert: connecting points to nanoelectrodes) (B) Microchannel mask (insert: zoom in to view)

One-hundred nanometer deep trenches were created by exposing the coated substrate to a Lab Star TTL model ICP-RIE with the following conditions; CF_4 = 10 sccm, CHF_3 = 45 sccm, Ar = 10 sccm, pressure = 150 mTorr, power = 150 W, time = 200 s. Next, the resist was removed by soaking in piranha solution for 10 min followed by cleaning and drying the wafer. Electrodes consisting of 10 nm thick Cr serving as an adhesion layer and 40 nm Au layer were electron-beam evaporated into the trenches using a WOOSUNG e-beam evaporator-1 (DC voltage = 8.90 kV) with deposition rates of 1.5 Å/s and 1.0 Å/s for Cr and Au, respectively. After deposition, there was still a 50 nm space left between the electrode and the quartz surface. This was used to allow for

the deposition of the nanoelectrodes, which were 45 nm in thickness, to allow for ease of bonding the substrate to a cover plate.

3.1.2 Nanoelectrodes (Steps 3-4, see Scheme 3.1)

For the nano-electrodes, a 100 nm layer of the e-beam resist (Zep520A) was spin coated onto the fused silica wafer at 1,500 rpm. When undertaking e-beam lithography (EBL) on a non-conductive substrate, charge will build up on the substrate during exposure causing broadening of the structures. Therefore, a 50 nm layer of Al was deposited on the resist using chemical vapor deposition (CVD). This Al layer had a negligible effect on the forward scattering of electrons during EBL and minimized charging artifacts. The Cr alignment marks were again used to align the substrate with respect to the EBL mask. The e-beam writing was performed using an ELS-7000 e-beam writer operating at 100 keV and a current of 30 pA. It took approximately 0.2 s to write 30 nm x 30 nm patterns (12) on a 0.5 mm quartz wafer. After removing the Al layer, the resist was developed using an O-Xyele developer for 1 min. The nano-patterns were then etched into the substrate using ICP-RIE running with the following process conditions: pressure = 150 mTorr, CF_4 = 10 sccm, CHF_3 = 45 sccm, Ar = 10 sccm, power = 150 W and time = 100 s. The nanoelectrodes consisted of a 10 nm Cr adhesion layer and 35 nm Au layer that were electron-beam evaporated using the WOOSUNG e-beam evaporator-1 running at a DC voltage of 8.90 kV with deposition rates of 1.5 Å/s for Cr and 1.0 Å/s for Au. Of the 12 devices poised on a single wafer, several had a spacing of 30 μm between the nanoelectrodes while the others had a 40 μm spacing. Resistance measurements across the contact pads were used to verify electrical continuity between the micro- and nano-electrodes.

3.1.3 Microchannels (Step 5, Scheme 3.1)

After electrode fabrication, microchannels were fabricated onto the wafer. Optical lithography and ICP-RIE were used to fabricate these structures. Prior to coating a photoresist, the wafer containing the micro and nanoelectrodes was coated with a 1 μm thick Al layer, which served to minimize charging during RIE. The wafer was spin coated at a speed of 3,000 rpm for 30 s with the photoresist consisting of nLOF2035. The coated wafer was pre-baked at 105^0C for 2 min. Next, the wafer was aligned with respect to the mask (Figure 3.3B) on the SUSS MICROTEC MA6 mask aligner and patterned by exposure to UV light at 90 mJ/cm^2. The photoresist was subjected to a post exposure bake at 110^0C for 2 min followed by development for 2 min in an AZ300MIF developer. The patterned substrate was then etched using the SNTEK ICP1000 etcher with working conditions of C_4F_8 = 80 sccm, O_2 = 10 sccm, power = 1,300 W and time = 15.5 min. Fifty μm wide and 8 μm deep microchannels were created. The etched substrates were then cleaned in piranha solution and DI water for 10 min each, and finally air dried for 5 min.

3.1.4 Access Reservoirs (Step 6, see Scheme 3.1)

Access reservoirs were generated by etching 1.5 mm reservoirs from the backside of the quartz wafer using powder blasting. The holes were 1.0 mm in diameter and were produced using 110 μm Al_2O_3 particles incident on the substrate at an angle of 80^0 through a nozzle with compressed air. The etching time was ≤10 s per reservoir. A 70 μm adhesive Nitto SWT 20 tape was used as the masking material. The positions of the inlet reservoirs were pre-marked on the tape by ablation.

3.1.5 Dicing (Step 6, see Scheme 3.1)

A single wafer accommodated a total of 12 chips (Figure 3.2). The subsequent FIB milling step requires that each chip be milled at a time. It is therefore important to cut out each chip from the quartz wafer substrate. The quartz wafer in our experiment was diced along the designed saw lines demarcating each chip. This was done using a 200 μm graphite edge blade running at a spindle speed of 20,000 rpm and cutting speed of 1mm/sec. Each chip of size 20 mm x 20 mm was carefully cut from the wafer.

3.1.6 Funnel/Nanopillar Input, Nanochannel and Nanogap Formation: Focused Ion Beam (FIB) Milling (Step 7, see Scheme 3.1)

To prevent charging of the insulating substrate during focused ion beam milling to produce features with nanometer dimensions, the substrate surface was coated with a thin conductive metal layer, which in this case consisted of a 100 Å thick Al layer deposited over the entire chip using an e-beam evaporator operating under the same conditions as discussed for the nano-electrode fabrication. The FIB milling beam current was controlled and optimized as reported by Menard *et al.*[1] to ensure that the nanochannels and nanopillars were of the intended dimensions. The Al-coated device was loaded into the Quanta 3D FEG FIB with carbon tape serving as the non-conductive bottom and copper tape connecting the conductive top to the stage. The funnel entrance and nanopillars were milled at the edge of one of the microchannels (see Figure 3.1) using a bitmap application. The FIB etch mask was designed using AutoCAD and uploaded as a bitmap file to the FIB machine. The funnel entrance had a length of 20 μm from tip to base and was populated with staggered circular nanometer-sized pillars of about 150 nm in height, 350 nm diameter and 150 nm edge-to-edge

spacing. A single 50 nm x 50 nm nanochannel was milled from the apex of the funnel, across the nanoelectrodes and to the opposite microchannel. This process created not only the nanochannel, but the nanogap between the electrodes. Complete cutting of the nanoelectrodes by the FIB was verified by resistance measurements made across the contact pad using a multimeter.

3.1.7 Wafer Cover Plate Bonding (Step 8, see Scheme 3.1)

Alkali-assisted bonding was used to seal the cover plate to the substrate containing the fluidic network and electrodes. All bonding steps were done in a wet station of the clean room. Before bonding, a 25 mm x 25 mm x 0.17 mm commercial quartz cover plate was cut in two (25 mm x 12.5 mm plates) using a diamond cutter. This was done to ensure that the contact pads were uncovered after the device had been assembled to allow metal contact to nanoelectrodes while still ensuring that the access holes were completely sealed. The substrate and cover slip were first pre-cleaned in piranha solution for 10 min. Piranha solution not only served to remove the Al conductive layer from the substrate, but also removed organic contaminants from both the substrate and cover plate. Piranha cleaning was followed by complete flushing with water for 5 min and air drying for 5 min. For successful bonding of the quartz cover plate to the substrate, the hydrophobic surfaces must be made hydrophilic. This was achieved by immersing the substrate in 29% NH_4OH at 55^0C for 30 min and the cover slip in 50% KOH at 85^0C for 8-10 min. Next, the treated substrate and cover plate were flushed with deionized water for 5 min and dried with N_2 gas for 5 min. The dried substrate was then placed on a dry kim-wipe with the patterned side facing up and the cover plate was quickly brought into contact with the substrate. The assembly was then

gently pressed together from the center towards the edge of the cover slip so as to eliminate trapped air bubbles, the presence of which were observed through the appearance of Newton rings. To improve the bond strength, the assembled device was pressed together overnight with a 5 lb weight. Thermal heating was avoided to prevent delamination of the Au electrodes and possible collapse of the nanochannel at temperatures close to the glass transition temperature (T_g) of the quartz substrate. Good bonding was confirmed by performing a sealing test, which consisted of filling the fluidic channels with 5 μM FITC and visualized using an epi-fluorescent microscope with a 100X objective.

3.2 Electrical Property Testing of Nanoelectrodes

To ensure that solutions gained easy access to the fluidic channels of the device and that there was a pressure balance when filling the channels, a 0.5 cm thick PDMS (20 mm x 12 mm) slab with four 2.5 mm sized circular holes was bonded to the back side of the device. 0.5X TBE buffer was allowed to fill the channel network and was used to monitor the electrical properties of the device. The buffer solution was introduced into the microchannels while the nanochannel was allowed to fill by capillary action. A low pressure vacuum pump was used to eliminate any trapped air bubbles within the channels. Longitudinal and transverse currents were monitored as a function of bias voltage and I-V plots were generated for each case. An Axopatch 200B amplifier coupled to a CV headstage connected to platinum electrodes was used as the voltage follower. A Digidata 1440A served as the Analog-to-Digital and Digital-to-Analog (AD/DA) converter. Data acquisition and analysis was performed using the pCLAMP 10 software sampling at a rate of 10,000 Hz.

3.3 References

1. Menard, L. D.; Ramsey, J. M., Fabrication of Sub-5 nm Nanochannels in Insulating Substrates Using Focused Ion Beam Milling. *Nano Lett.* 2010, null-null.

CHAPTER 4. RESULTS, DISCUSSIONS, CONCLUSIONS AND FUTURE WORK

This chapter focuses on the results obtained while developing the fabrication scheme for our integrated device and the electrical properties of the nanogap device. Herein, we supply Scanning Electron Micrograph (SEM) images showing the outcome from each stage of our fabrication scheme. We have also described the electrical behavior of the device and provided an insight into the prospects of using our device as a DNA sequencing tool.

4.1 Results and Discussions

4.1.1 Microchannel Fabrication

Figure 4.1 shows SEM images of test microchannels fabricated in a bare quartz substrate at the optimum conditions. First, we prepared an AutoCAD file, which specified the intended dimensions of the microchannel as 6 mm x 50 μm x 7 μm (length x width x depth). The channels were terminated by 1 mm diameter access reservoirs at both ends. Next, the photolithographic mask was machined based upon the designed dimensions and finally, the experimental conditions for the optical lithography and ICP-RIE were optimized. At these conditions, the resulting microchannels with cross sectional area of 3.31×10^{-4} mm^2 (dimensions; 5.86 mm x 48.87 μm x 6.78 μm - see insert in Figure 4.1) were successfully produced.

4.1.2 Input Funnel/Nanopillar and Nanochannel

Previous reports have stated that entropic and electric field barriers prevent single DNA molecules from entering a nanochannel without the application of a large driving voltage. We have found that a funnel nanochannel entrance can induce efficient entry of single molecules into a nanochannel without the need of a high bias voltage.

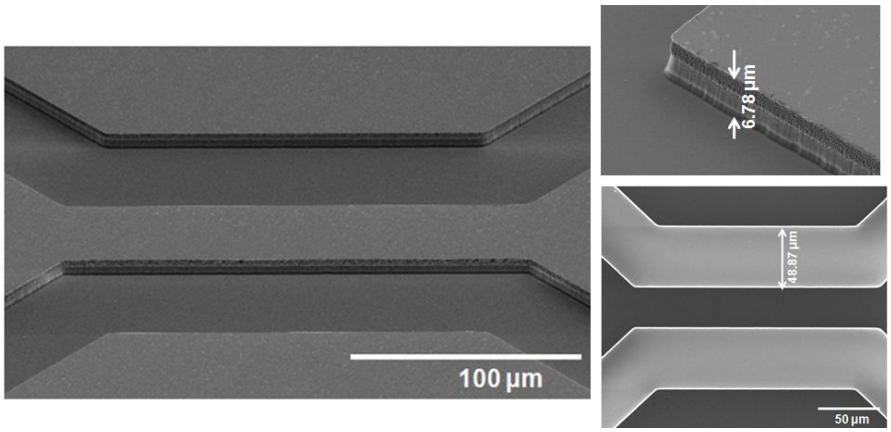

Figure 4.1 Left panel - SEM image showing two opposite microchannels fabricated in quartz substrate using the conventional optical lithography and ICP-RIE. Upper right panel – shows microchannel depth of 6.78 µm; Lower right panel – on axis SEM image showing a microchannel width of 48.87 µm.

Recently, Kaji N *et al.*[1] successfully stretched and separated a mixture of DNA molecules by passing them through a microchannel populated with an array of staggered nanopillars 500 nm in diameter and edge-to-edge separation. Based on this report, we FIB machined a 50 nm x 50 nm nanochannel with a funnel input populated with nanopillars. This input funnel will aid in DNA stretching and allow for low electric fields introduction of DNAs into the nanochannels from microchannels feed channels. The final dimensions of the input funnel, nanopillar and nanochannel array were optimized by controlling the thickness of the Al conductive layer. The FIB milling conditions were based on the report of Menard *et al.*[2] The milling current used in all cases was 30 pA while the metal layer thickness was between 200 – 400 Å.

Two funnel/nanopillar input configurations were fabricated. The first configuration was shaped like an equilateral triangle and largely populated with staggered nanopillars (see Figure 4.2A). The second configuration was shaped like a tapered cone but was populated with less numbers of nanopillars (see Figure 4.2B). The large population of

nanopillars in the former would allow for better stretching and also separation of a mixture of long DNAs. This makes our integrated device useful as an analyzer for a mixture of biopolymers, like DNAs of various lengths. Both configurations have nanopillars with diameters = 349.7 nm, forward and backward spacing = 163.3 nm, edge-to-edge spacing = 145.8 nm and height = 151.5 nm (see Figure 4.2C and D). Finally, a single 2-D nanochannel (50 nm x 50 nm), shown in Figure 4.2E, was machined to connect the apex of the funnel inlet to the opposite microchannel. The entire assembly is shown in Figure 4.2F.

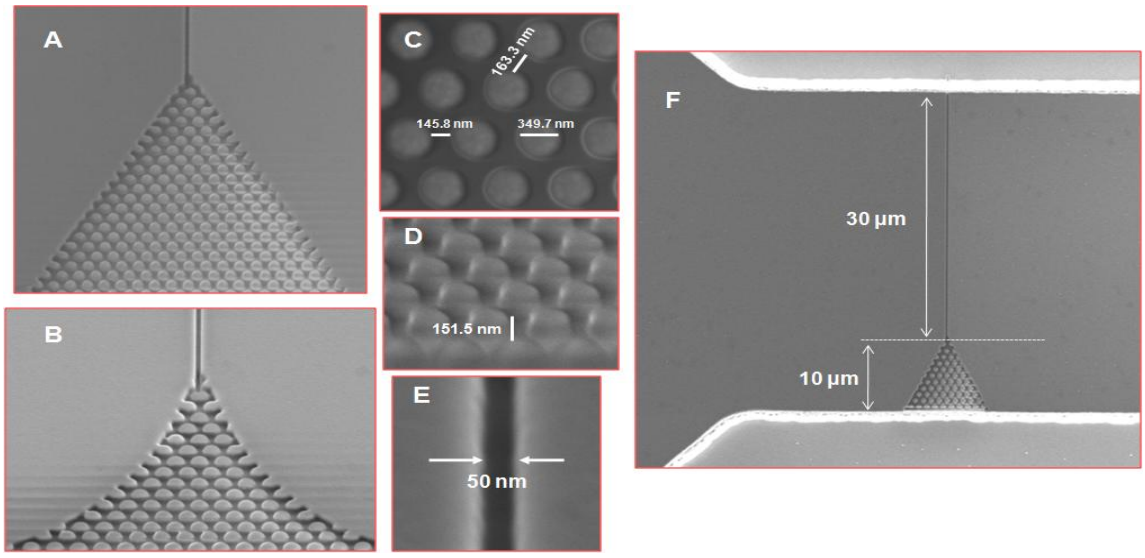

Figure 4.2 Entrance funnel (A) like an equilateral triangle and populated with a large number, and (B) like a tapered cone with fewer numbers of nanopillars. (C) Top view of nanopillars with diameter ~350 nm, forward and backward spacing of ~160 nm and side spacing of 145 nm (**D**) Image showing the nanopillar height of ~150 nm. (**E**) Nanochannel of width 50 nm (**F**) Funnel/nanopillar/nanochannel configuration in quartz substrate. The nanochannel has a length of 30 µm while the funnel entrance is 10 µm long.

4.1.3 Fabricating One-Dimensional Nanoelectrodes

Although we aimed to pattern electrodes with a size of 50 nm x 50 nm, it was important to optimize the fabrication conditions for the microelectrodes and the contact pads and to understand the electrical behavior of nanogaps; therefore, 2 µm wide and

~55 nm deep electrodes were fabricated in the quartz substrate. Figure 4.3A shows an AFM image of the patterned quartz substrate before e-beam evaporation. The depth of the pattern was 54.2 nm (see Figure 4.3B). After e-beam evaporation of Cr/Au (10 nm/40 nm), the measured electrical resistance across the electrode was 150 $\pm$ 3 Ω.

Next, microchannels were etched into the substrate containing these electrodes. Figure 4.4A (upper panel) shows an SEM image of the fabricated 2 μm wide electrodes with the associated fluidic network. The electrodes were cut by FIB milling to produce a nanogap of ~54 nm (Figure 4.4A – lower panel) as well as the nanochannel.

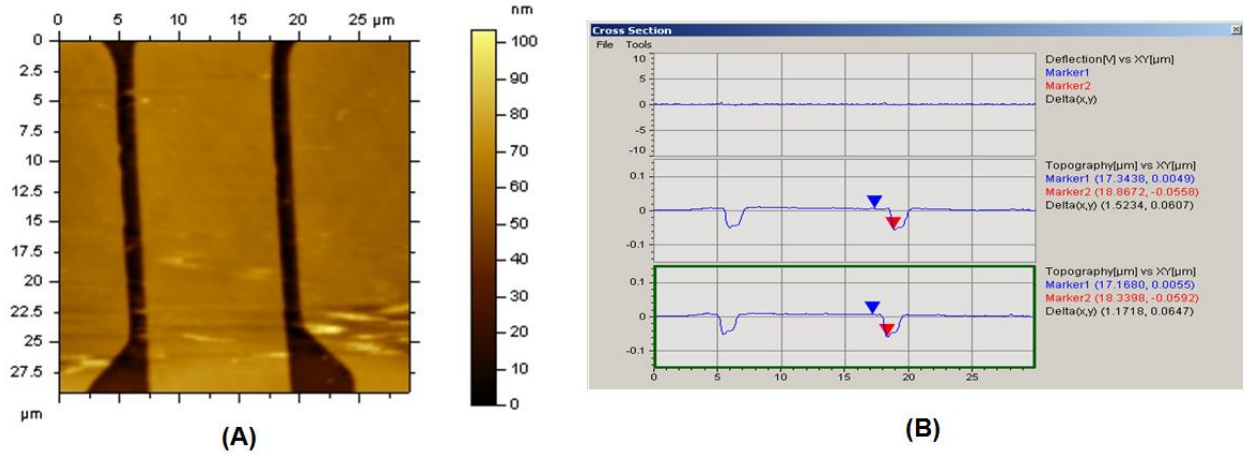

Figure 4.3 (A) AFM image of the patterned quartz substrate (B) AFM profile showing the depth of the pattern to be about 54.2 nm

The depth of the nanogap was investigated by depositing Pt transversely across the Au electrodes followed by cross-section analysis with the FIB. The deposited Pt filled the nanogap and created a contrast that allowed for easy imaging of the cross-section. As shown in Figure 4.4B, the depth of the nanogap was 77.2 nm. Electrical resistance measured across the machined electrode was infinite, confirming complete cutting.

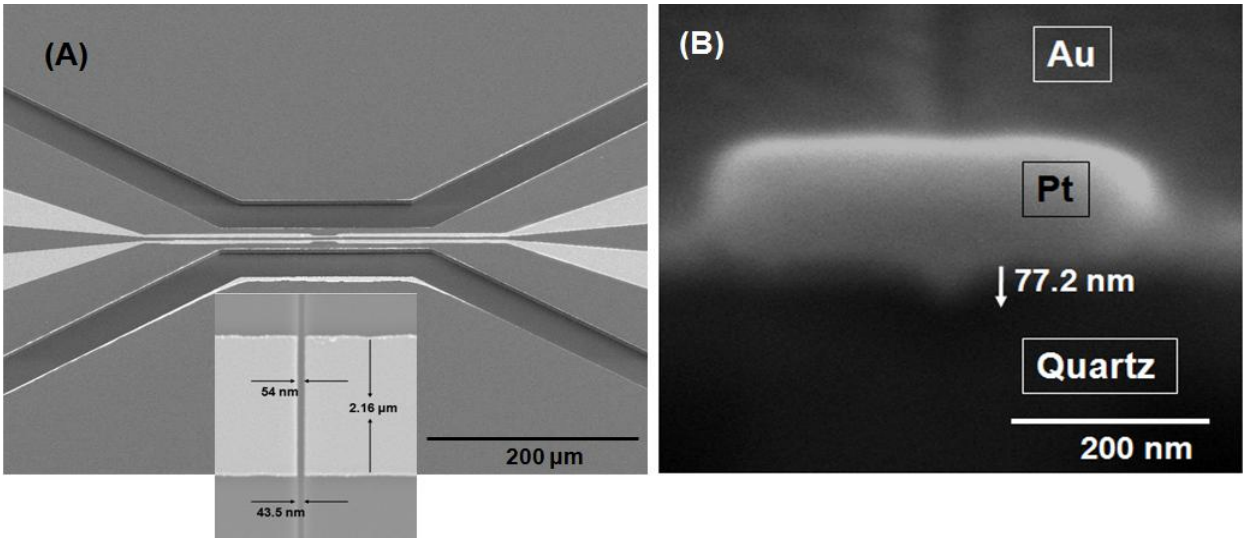

Figure 4.4 (A) Upper panel - Nano-sensor for reading the identity of single mononucleotides clipped from a dsDNA molecule. The electrodes are made from Au and the image shows both the microchannels and nanochannel. Lower Panel – 54 nm gap between Au nano-electrodes of width 2.16 µm. (**B**) Shows Pt deposition across the nanogap followed by a cross-section. Pt creates a contrast and allows for easy imaging. The depth of the nanogap was 77.2 nm.

4.1.4 Fabrication of Two-Dimensional Nanoelectrodes

Next, we scaled down the electrode size to the nanometer regime following the steps described in section 3.1.2. Initially, we encountered some problems while trying to deposit the Au electrodes into the nanopatterns. These problems arose due to the fact that the quartz wafer initially had access reservoirs powder blasted in them prior to embarking on the nanopatterning steps. This resulted in non-uniform coating of the e-beam resist on the wafer. It also made it difficult for the vacuum system of the e-beam evaporator to hold the wafer in place. Figure 4.5A shows an SEM image of a poorly fabricated nanoelectrode. No contact was observed between the micro-electrodes.

To create the contact between these electrodes, we deposited nanometer lines of platinum between the microelectrodes using the Gas Injection System of the Quanta 3D FIB at 30 pA beam current. Figure 4.5B shows an SEM image of deposited 400 nm

wide and 70 nm deep Pt metal electrodes. The electrical resistance across the electrodes after removal of the metal layer was 7.96 kΩ. This large drop in electrical resistance confirmed connection. Next, a nanochannel of 40 nm wide and 85 nm deep was machined across the nanoelectrode (see Figure 4.5C) to create the nanogap. The electrical resistance of the machined substrate when measured was found to be infinite. This became an alternative approach for the fabrication of our nanoelectrode.

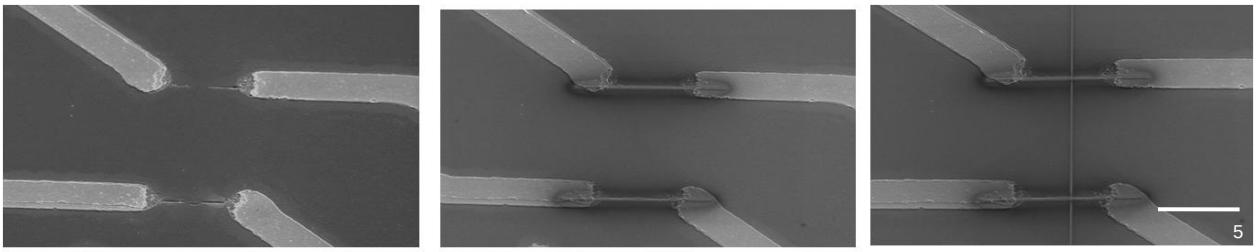

Figure 4.5 (A) SEM image showing a poorly fabricated nanoelectrode (B) Image of the 400 nm x 70 nm Pt electrode across the microelectrodes (C) Image of a 40 nm x 90 nm nanochannel machined across the nanoelectrodes. Complete cutting was observed by a significant change of the resistance to infinity.

Finally, the entire fabrication scheme was implemented and our nanogap device was generated. The device we fabricated had an electrode size of 100 nm x 80 nm with nanogap sizes of ~50 nm. The inlet funnel was about 20 μm in length and populated with nanopillars of 120 nm in height. Figure 4.6 shows the SEM image of the device. The insert shows the nanoelectrode and nanochannel with a width of 45.1 nm.

4.1.5 Chip Assembly

After fabrication of the electrodes and nanochannel, the final step consisted of device assembly. This involved bonding the patterned quartz substrate to a cover plate made from the same material. Several methods have been reported for bonding quartz substrates. Commonly used methods involve thermal fusion bonding at temperatures close to the glass transition temperature of quartz (1,100^{0}C) for 7 h.[3, 4]

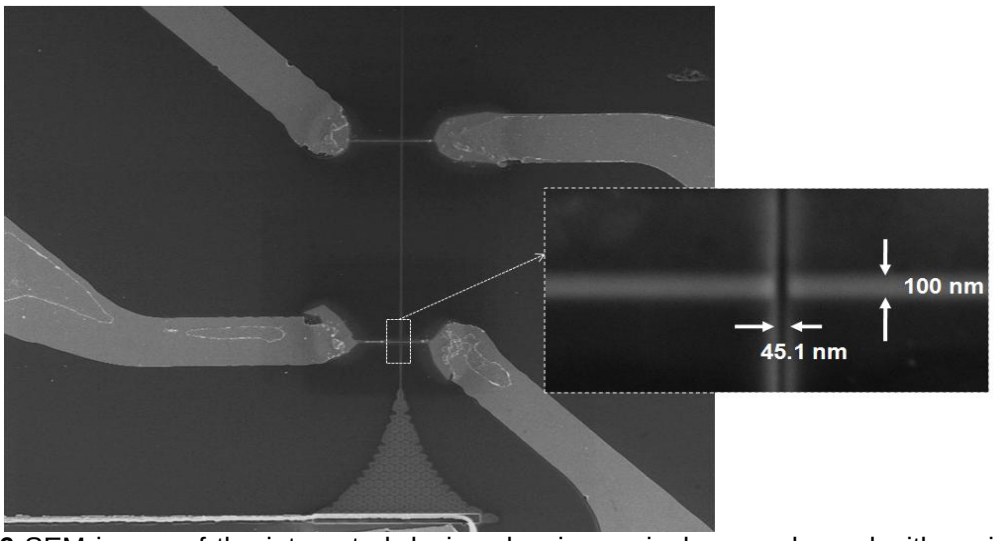

Figure 4.6 SEM image of the integrated device showing a single nanochannel with an inlet funnel populated with nanopillars cutting across the nanoelectrodes. Insert shows the 100 nm nanoelectrode with connected to nanochannel of 45.1 nm width.

Furthermore, a recent bonding method developed by Menard *et al.*[2] to seal quartz substrates with 2-D nanochannels involved treating both surfaces with oxygen plasma followed by thermal bonding at 900^0C for 6 h. Although, these bonding methods offered a high yield, bonding our device at temperatures close to the T_g run the risk of collapse of the nanochannel and nanopillar structures as well as delamination and degradation of the nanoelectrode as well as the microelectrodes. We tested the approach reported by Menard *et al.,* however, we observed delamination of the Au electrodes. Figure 4.7A and B shows SEM images of the chip before and after heating, respectively. The delamination was due to the difference in the coefficients of linear expansion of Au and Cr relative to quartz (Au = 14.2×10^{-6} K^{-1}; Cr = 6.2×10^{-6} K^{-1}; Quartz = $(0.77 – 1.4) \times 10^{-6}$ K^{-1}).

Next, non-thermal bonding methods were tested. We activated the surfaces of both the substrate and the cover plate in 45% KOH solution at a temperature of 85^0C for 15 min followed by spontaneous fusion bonding at room temperature. Although we

achieved good bonding in this case, we noticed a significant increase in the nano-channel width after KOH treatment. There was ~350% increase in the width of the nanochannel, from 242.50 $\pm$ 4.50 nm to 1092.5 $\pm$ 28.98 nm, but no significant change in the depth resulted (317.43 $\pm$ 8.60 nm to 323.1 $\pm$ 10.70 nm). SEM images taken before and after KOH treatment are shown in Figure 4.8A and B, respectively. In addition, we observed delamination of the electrodes after KOH treatment.

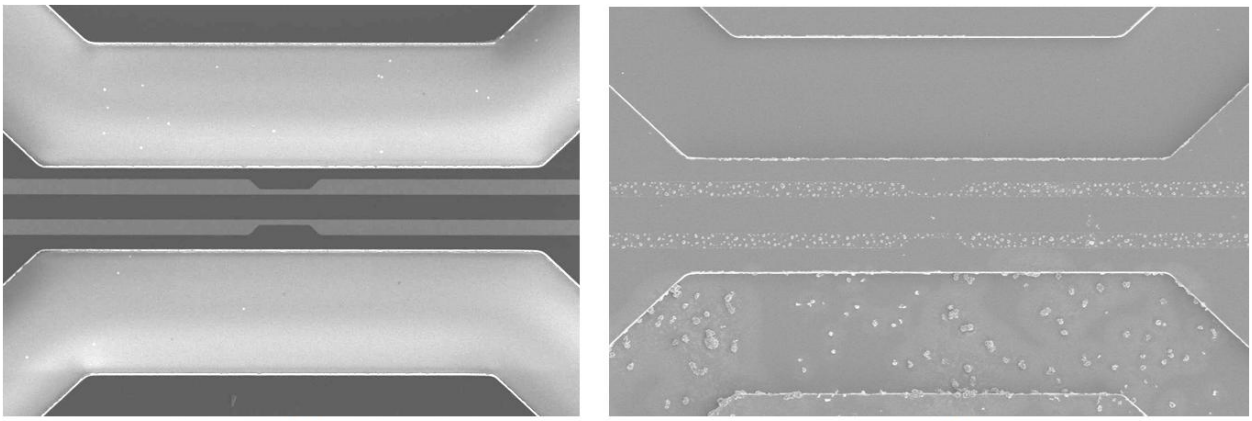

Figure 4.7 SEM images showing changes in thin film of Au in quartz substrate (A) before and (B) after heating in a furnace up to 900^0C for 6 hours.

Subsequently, we tested the fusing bonding scheme reported by Mao *et al.*[5] for sealing quartz nanofluidic chips using 29% NH_4OH. We found that soaking the substrate in an NH_4OH solution at 55^0C for 30 min had no effect on the electrodes. This was confirmed by measuring the electrical resistance across a treated sample without the nanochannel. SEM imaging of the NH_4OH treated substrate showed that there was no damage to the nanochannel after treatment with NH_4OH as well, however, after the assembly of the device, the bonding was weak. This was evident by separation of the substrate from the cover plate after the filling with buffer solution.

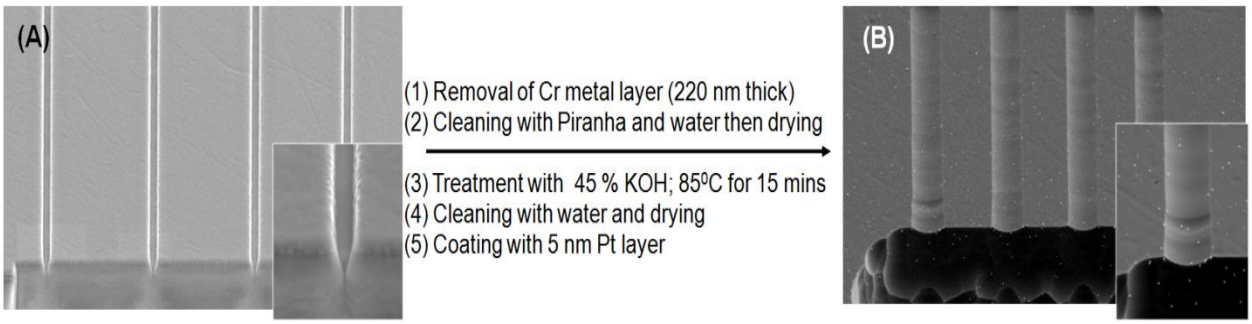

Figure 4.8 (A) SEM image of the nanochannels fabricated in quartz substrates coated with a 220 nm Cr layer (Insert: zoomed in view of the nanochannel depth) (B) SEM image of the nanochannels after performing the experimental procedure shown in the figure. There was ~350 % increase in the width from 242.50 ± 4.50 nm to 1092.5 ± 28.98 nm but no significant change in depth 317.43 ± 8.60 nm to 323.1 ±10.70nm.

Finally, we modified the bonding scheme by Mao *et al.*;[5] in this case, the substrate was activated with NH_4OH while the cover plate was treated with KOH. Both surfaces were then brought into conformal contact and pressed together with a 5 lb weight overnight. A PDMS slap was plasma bonded to the back side to create the extended reservoirs (see Figure 4.9A).

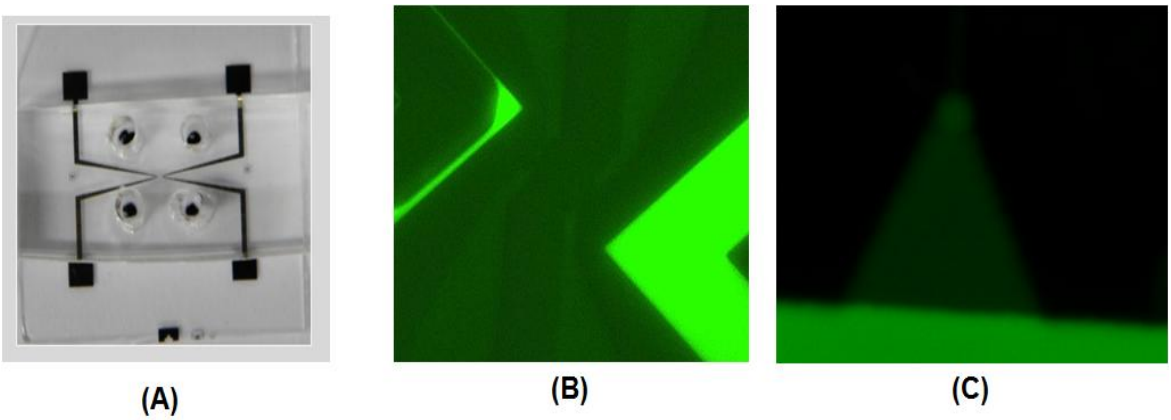

Figure 4.9 (A) Photograph of the assembled integrated nanogap device (B) Fluorescence image of the microchannels at 40X magnification showing the fluorescent seeding of 5 µM FITC across the nanochannel (C) Z-stack fluorescence image of the entrance funnel visualized with the 100 X objective lens of the confocal microscope.

The assembled device was tested for good sealing using a 5 µM FITC in 1X TAE buffer serving as the seed solution. The dye was introduced into one microchannel

(microchannel on the right in Figure 4.9B) and allowed to fill the nanochannel by capillary action. After approximately ~3 min, there was fluorescence observed from the opposite microchannel (on the left in Figure 4.9B). Figure 4.9C shows the z-stack fluorescence image of the funnel input acquired using a 100X objective of a fluorescence confocal microscope.

4.1.6 Electrical Operation

An Axopatch 200B amplifier operating with a head stage gain of 1mV/pA and bandwidth of 140 kHz was used to test the electrical properties of the nanogap device. Although the noise rms level was 0.14 pA at 100 kHz sampling rate, there was external noise leading to a peak-to-peak baseline current for a 0.5X TBE of about 200 pA with 60 Hz AC noise. To reduce this contribution, the entire set up was housed in a grounded Faraday casing shown in Figure 4.10 (right). Grounding reduced the peak-to-peak noise by 100-fold, from 200 pA to 2 pA, and completely eliminated the 60 Hz noise. The sample chamber (see Figure 4.10 left) was demarcated from the amplifier itself and from external noise from other sources.

Before filling the device with 0.5X TBE, the tunneling current across the nanogap device was monitored. This is shown in Figure 4.11A. The device was filled with 0.5X TBE buffer and current-voltage (I-V) plots were generated. The traces in Figure 4.11B **I** and **II** reveals the I-V plot across the transverse input and output electrodes, respectively. Also, the longitudinal current was monitored along the length of the nanochannel (see Figure 4.11B **III).** Linearity of all plots suggested ohmic behavior across the nanogap and along the length of the nanochannel in the voltage range of 0 –

1 V. Reliable quantitative data can be acquired across the nanogap at this working voltage range.

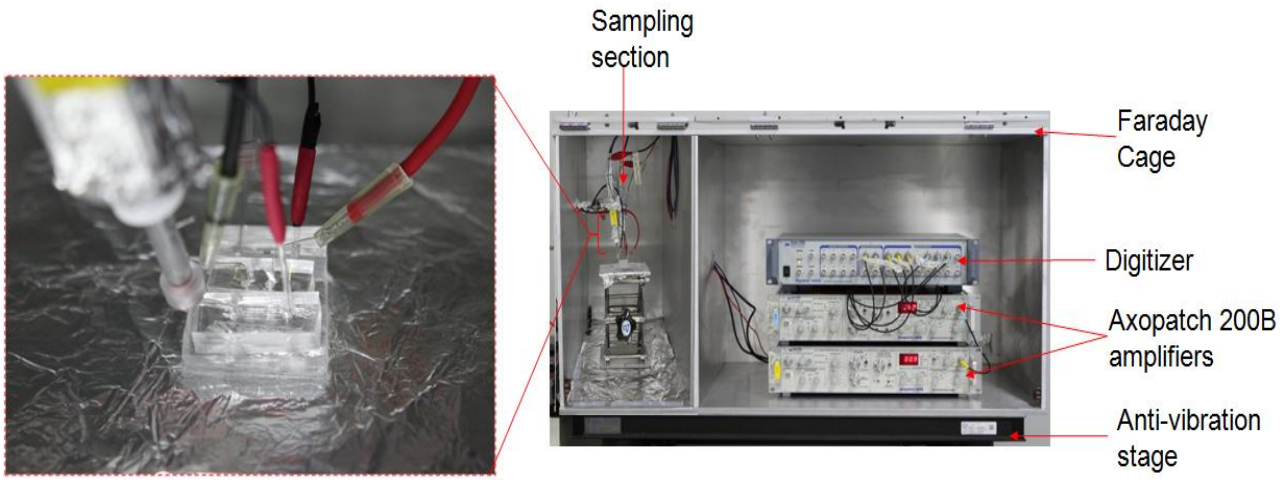

Figure 4.10 Photograph of the Set-up of the actual experiment. Shown on the right are the Axopatch amplifiers and the digitizers kept in a Faraday cage to reduce the noise as much as possible. The photograph on the right is the zoomed in view of the sample section showing the contacts to the headstage of the amplifier.

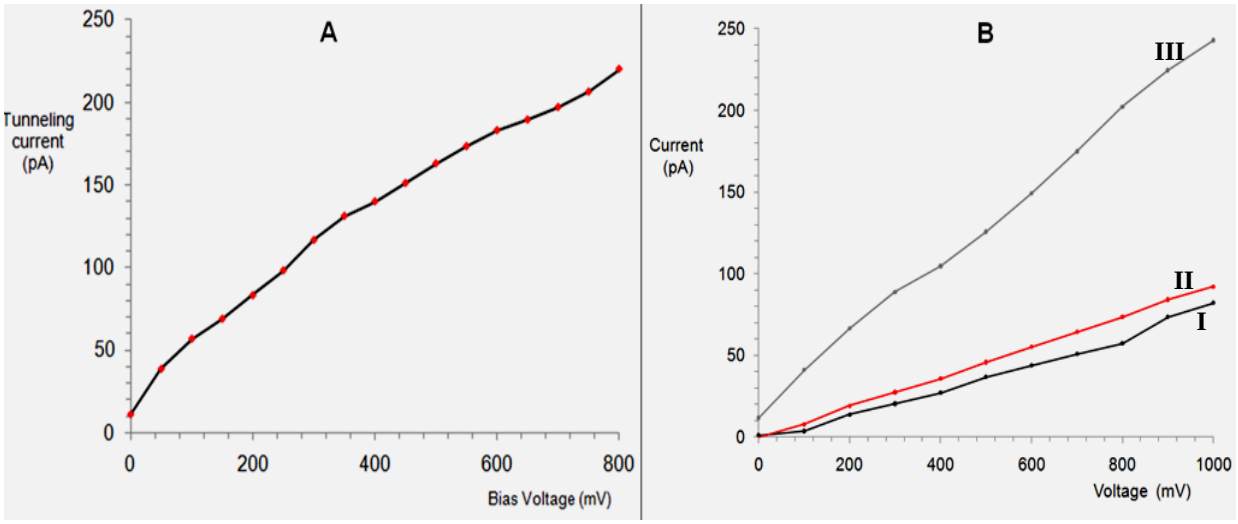

Figure 4.11 (A) Variation of tunneling current across the 2 µm electrodes and 50 nm wide nanogap with the bias voltage. (B) I-V plots across the channel filled with 0.5X TBE. I and II represent the I-V plots measured transverse to the nanochannel across the input and output electrodes, respectively; **III** represents the I-V plot measured longitudinally across the nanochannel.

4.2 Conclusions

In this project, we successfully fabricated a nanosensor platform in quartz that will serve as the foundation for a non-labeling novel DNA sequencing system based on Time-of-Flight (ToF) measurements of single mononucleotides clipped from a double-stranded DNA biopolymer digested with a λ-exonuclease enzyme. The integrated fluidic system was comprised of a nanofluidic channel (50 x 50 nm, width x depth) containing two pairs of transverse Au nano-electrodes poised at the input/output ends of the nanochannel. The nanochannel also possessed a funnel entrance populated with nanopillars to reduce entropic barriers and allow efficient entry of single molecules.

Electrode pairs were poised orthogonal to the nanochannel with a gap ~50 nm situated between them to measure current perturbations induced when single molecules travel through them. Our device measures the change in conductivity in the detection volume defined by the size of the nano-scale electrodes and gap between them. The identity of the molecular entity is determined by its different interaction times with the channel wall, which determines the magnitude of the flight time (i.e., single-molecule chromatography). The nanochannel wall serves as the chromatography column to provide the molecular-dependent flight times of single-molecules electrokinetically driven through this column.

The entire fabrication procedure was accomplished using a unique chain of procedures in a clean room environment. Eight different processing steps were required and generally involved micro-patterning (optical lithography, e-beam evaporation, reactive ion etching) and nano-patterning (electron beam lithography, FIB milling and reactive ion etching). Resistance measurements across the electrodes were used to

check for successful deposition and cutting of the electrodes. A seeding solution consisting of a fluorescent dye and confocal fluorescence microscopy were used as a sealing test to assure that the cover plate was successfully bonded to the substrate. The electrical property of the device was investigated and was found to be ohmic in behavior in the working voltage range 0 – 1 V.

4.3 Future Work

Nano-scale fluidic devices provide opportunities to perform unique measurements, such as single-molecule sequencing. It will be interesting to take our work a step further into the area of sequencing of biopolymers, like proteins and DNA.

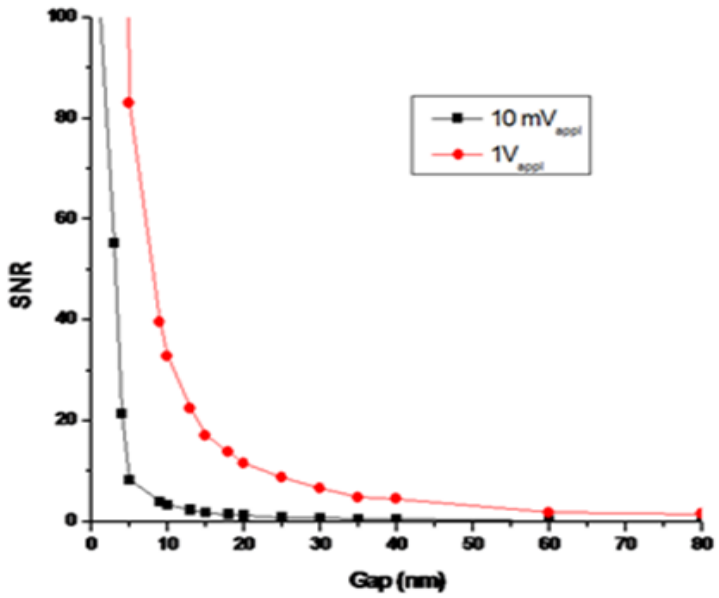

Figure 4.12 Variation of SNR with the nanogap size for cytochrome c molecule traveling across the gap between 40 nm x 40 nm electrodes. Red line shows the variation with a 1V bias voltage; Black line shows the variation with 10 mV bias voltage.

Theoretical computations performed to check the variation of the signal-to-noise ratio with nano-gap size for Cytochrome C and mononucleotides reveal that the prospect for this identification protocol is viable. These computations were based on 40

nm x 40 nm nanoelectrode size and 0.5X (pH 7.5) TBE buffer (see Figure 4.12 for data on Cytochrome c (size ≈ 506 nm^3) and Table 4.1 for data on the transduction of DNA mononucleotides (size ≈ 1 nm^3)). Different functional groups can be generated within the channel and the information about ToF of single molecules in variation with the EOF and potential wall interactions can be obtained to aid in ToF identification of single molecules.

Table 4.1(Right) Variation of the electrical signal with the nanoelectrode and nanogap sizes for single mononucleotide units. There is an increase in the signal as the volume of the detection window reduces.

Electrode size (nm x nm)	Nanogap (nm)	ΔI ($x 10^{-12}$ A)
10 x 10	5	20
5 x 5	5	23
3 x 3	5	22.5
2 x 2	5	22.5
10 x 10	3	63
5 x 5	3	62
3 x 3	3	62
2 x 2	2	140

Furthermore, it will be interesting to monitor single molecule perturbations across our nanogap detector and transduce these perturbations to ToF measurements. Devices with nanoelectrode gap size ≤10 nm can be fabricated to monitor perturbations from protein molecules while a gap size ≤3 nm would be necessary for mononucleotide measurements. In addition, the effect of the surface chemistry within the nanofluidic channel on the ToF from single molecules is also an important phenomenon that needs

to be investigated. As the molecules travel through the nanochannel, they can interact with the walls of the channels. A change in the surface functional groups within the nano-channel will translate into a change in the EOF within the channel, hence, a corresponding change in the ToF of the single molecule traveling through the channel.

4.4 References

1. Kaji, N.; Tezuka, Y.; Takamura, Y.; Ueda, M.; Nishimoto, T.; Nakanishi, H.; Horiike, Y.; Baba, Y., Separation of Long DNA Molecules by Quartz Nanopillar Chips under a Direct Current Electric Field. *Anal. Chem.* **2003,** *76* (1), 15-22.
2. Menard, L. D.; Ramsey, J. M., Fabrication of Sub-5 nm Nanochannels in Insulating Substrates Using Focused Ion Beam Milling. *Nano Lett.* **2010**, null-null.
3. Jacobson, S. C.; Moore, A. W.; Ramsey, J. M., Fused Quartz substrates for microchip electrophoresis. *Anal. Chem.* **1995,** *67* (13), 2059-2063.
4. Becker, H.; Lowack, K.; Manz, A., Planar quartz chips with submicron channels for two-dimensional capillary electrophoresis applications. *Journal of Micromech. and Microeng.* **1998,** *8* (1), 24-28.
5. Mao, P.; Han, J., Fabrication and characterization of 20 nm planar nanofluidic channels by glass-glass and glass-silicon bonding. *Lab on a Chip* **2005,** *5* (8), 837-844.

VITA

Franklin I. Uba received his Bachelor of Science in Industrial Chemistry (First Class honors) from the University of Ibadan in 2007. His undergraduate research work focused on paper making from *Carpolobia lutea*. After graduation, he joined the Petroleum Chemistry program of the American University of Nigeria (AUN) as a graduate assistant. Around this time, Franklin was involved in full time teaching of classes and labs in polymer, organic and analytical chemistry. He also worked with the AUN faculty team on Crude oil finger-printing and quality control of petrochemicals for Nigerian oil companies. He joined the doctoral analytical chemistry program at Louisiana State University in the fall of 2009 and joined Prof. Steven A Soper research group in the spring of 2010. His current work focuses on studying the transport properties of nanometer sized assemblies through nanofluidic channels with single entity electrical detection and developing nanofluidic and nanogap based readout modalities towards single molecule detection and biopolymer sequencing. He is working on this project in collaboration with researchers in the World Class University at UNIST, South Korea, as a visiting student researcher.